University of Cincinnati

Date: 8/13/2015

I, Tyler R Fosnight , hereby submit this original work as part of the requirements for the degree of Master of Science in Biomedical Engineering.

It is entitled:

Echo Decorrelation Imaging of In Vivo HIFU and Bulk Ultrasound Ablation

Student's name: **Tyler R Fosnight**

This work and its defense approved by:

Committee chair: T. Douglas Mast, Ph.D.

Committee member: Syed Arif Ahmad, M.D.

Committee member: Marepalli Rao, Ph.D.

18381

Echo Decorrelation Imaging of *In Vivo* HIFU and Bulk Ultrasound Ablation

A thesis submitted to the
Graduate School
of the University of Cincinnati
in partial fulfillment of the
requirements for the degree of

Master of Science

in the Biomedical Engineering Program
of the College of Engineering and Applied Sciences
by

Tyler R. Fosnight

August 2015

Committee Chair: T. Douglas Mast (Chair)
Syed A. Ahmad
Marepalli B. Rao

Abstract

Echo decorrelation imaging, a pulse–echo method that maps heat-induced changes in ultrasound echoes, was investigated for *in vivo* monitoring of thermal ablation in a liver cancer model. In open surgical procedures, rabbit liver with implanted VX2 tumor were imaged by image-ablate arrays and treated with bulk ultrasound (unfocused) ablation (N=10) or high-intensity focused ultrasound (HIFU) (N=13). Echo decorrelation and integrated backscatter (IBS) images were formed from pulse-echo images recorded during rest periods following each sonication pulse. Echo decorrelation images were corrected for motion– and noise–induced artifacts using measured echo decorrelation from corresponding sham trials. Sectioned ablated tissue was vitally stained with triphenyl tetrazolium chloride (TTC) and binary images were constructed based on local TTC staining. Analysis was performed for the focused exposures, unfocused exposures and for all exposures combined.

Motion correction significantly reduced echo decorrelation in non-ablated liver regions. The reduction was significant in non–ablated VX2 tumor regions for focused exposures and all exposures combined. The reduction was not significant in ablated VX2 tumor regions for unfocused exposures. Echo decorrelation reduction was marginally significant in ablated regions for focused and unfocused exposures and was significant for all exposures combined.

In unpaired comparisons, echo decorrelation was significantly greater in ablated than in non–ablated liver regions but was not significantly greater in ablated than in non–ablated VX2 tumor. IBS was significantly greater in ablated than in non–ablated liver except for unfocused exposures. IBS was not significantly greater in ablated than in non–ablated VX2 regions. In paired comparisons, similar results were seen in comparison to the unpaired comparison; however, echo decorrelation and IBS were significantly greater in ablated than in non–ablated VX2 tumor for all exposures combined. Additionally, IBS was not significantly greater in ablated than in non–ablated liver for unfocused exposures.

Prediction of ablation by echo decorrelation and IBS imaging was assessed using receiver operating characteristic (ROC) curves. Areas under the ROC curve (AUC) were significantly greater than chance for ablated liver prediction by corrected echo decorrelation and IBS. Echo decorrelation did not predict ablated VX2 tumor significantly better than chance for focused exposures. IBS did not predict ablated VX2 tumor better than chance for focused exposures and unfocused exposures. Corrected echo decorrelation predicted ablated liver significantly better than IBS for the focused exposures and all exposures combined. AUC differences between corrected echo decorrelation and IBS were not significant for all exposure groups in ablated VX2 tumor, for which echo decorrelation was marginally higher. At the optimal threshold, defined as the threshold corresponding to the point nearest to the top left–hand corner of the ROC plot, echo decorrelation had a better sensitivity than specificity for the focused and unfocused exposures in normal liver and VX2 tumor.

To assess tissue motion effects due to large inter–frame times, echo decorrelation and IBS was computed for inter–frame times up to 847.5 ms. Uncorrected and corrected echo decorrelation prediction performance was marginally affected by large inter-frame times; however, corrected decorrelation was less affected. IBS prediction performance was nearly constant by comparison for large inter-frame times. Over the range of inter–frame times investigated, IBS predicted overall better than echo decorrelation for the unfocused group while echo decorrelation predicted overall better than IBS for the focused group.

These results indicate echo decorrelation imaging is a successful predictor of local ablation, with potential for real–time ultrasound system implementation and successful clinical translation. For most cases, echo decorrelation predicted ablated liver better than IBS and predicted ablated VX2 tumor marginally better than IBS. Tissue motion effects were shown to have little effect on echo decorrelation's ablation prediction performance; however, focused ablation prediction performance could potentially be enhanced by improving pulse–echo image resolution. Additionally, enhancement of prediction performance could be achieved by

leveraging three–dimensional volume ultrasound imaging systems, which inherently have slower frame rates, as echo decorrelation's performance was marginally affected by tissue motion. These results suggest that echo decorrelation imaging merits further investigation and has potential to improve real–time monitoring during HIFU thermal ablation and bulk ultrasound thermal ablation.

Acknowledgements

This work was supported by the National Institutes of Health (NIH) grant number R01-CA158439.

Words can't describe how thankful I am for all the grace and mentoring I received over the years from my graduate advisor Dr. T. Douglas Mast, my undergraduate advisors Dr. Christy Holland and Dr. Kevin Haworth, and everyone in the Biomedical Acoustics Laboratory and the Image-Guided Ultrasound Therapeutics Laboratories. Everyone has made great strides to shape me into a scientist/engineer with fortitude, temperance, good judgment, and prudence—and for that I am eternal grateful. I would also like to thank Dr. Marepalli Rao for his time and most importantly his help in developing the statistical analysis used in my thesis. I am also very grateful for Dr. Syed A. Ahmad for his clinical insight and his enthusiasm in propelling the clinical translation of my work. Thanks to all of my friends—without them I'm sure I would never smile. To my Mom and Dad—your love has been the fuel that's propelled me every second of the day and still fills my metaphorical tank. You've continuously reminded me to greet the dawn of each new day in ways which are best embodied by Kalidasa's poem:

SALUTATION TO THE DAWN
Look to this day!
For it is life, the very life of life.
In its brief course
Lie all the verities and realities of your existence:
The bliss of growth
The glory of action
The splendor of beauty,
For yesterday is but a dream
And tomorrow is only a vision,
But today well lived makes every yesterday a dream of happiness
And every tomorrow a vision of hope.
Look well, therefore, to this day!
Such is the salutation to the dawn.

Thank you all again!

TABLE OF CONTENTS

LIST OF FIGURES

Figure

LIST OF TABLES

Table

Chapter I

Introduction

1.1 Background and significance

1.1.1 Clinical significance

An estimated 35,660 new cases of liver cancer in the United States are expected in 2015 (Siegel et al., 2015). Hepatocellular carcinoma (HCC) will make up approximately 75% of these cases (Siegel et al., 2015). Of these new cases, 42% are expected to be diagnosed at an early stage, for which 5–year survival is 30% (Siegel et al., 2015). Approximately 80% of these patients will not be candidates for surgical resection or transplantation (Petrowsky et al., 2008).

HCC is a primary tumor of the liver that usually develops in the setting of chronic liver disease, particularly in patients with chronic hepatitis B and C, chronic alcohol consumption, NASH/NAFL (nonalcoholic fatty liver/nonalcoholic steatohepatitis), and Aflatoxin B1 or other mycotoxins (Bruix et al., 2005). Patients who develop HCC usually have no symptoms other than those related to their chronic liver disease (Bruix et al., 2005). Liver metastases (i.e., secondary tumors of the liver) are also a prevalent form of liver cancer and commonly originate from tumor sites in the breast, lung, and colon (Aubry et al., 2013).

The following sections will discuss treatment options and improvements for HCC, as other primary cancers of the liver [e.g., cholangiocarcinoma and bile duct cancer (Bruix et al.,

2005)] and secondary cancers of the liver may potentially benefit from similar treatments (e.g., thermal ablation).

1.1.2 Current treatment approaches

Resection, liver transplantation, and local nonsurgical therapies are options for early stage patients [i.e., patients who have fewer than 3 tumors smaller than 3 cm in diameter (Bruix et al., 2005)]. Surgeons can sometimes remove the tumor (i.e., resection or transplant); however, if the patient cannot undergo removal (e.g., if there are associated diseases), thermal ablation may be deployed (Bruix et al., 2005). This approach may also be used as an adjuvant therapy for transplant candidates to control tumor growth with the aim to extend the time to find a donor liver (Bruix et al., 2005). The aim of thermal ablation is to achieve malignant tumor death by delivering heat without damaging adjacent vital structures (Bruix et al., 2005). An ablative margin $\geq$5 mm around the entire tumor is often used to eliminate satellite foci of the disease and to overcome lesion boundary uncertainty (Nishikawa et al., 2013). A thermal dose can be determined using the empirical equation:

$$\mathrm{EM}_{43} = \sum R^{T(r)-43} \Delta t/60. \tag{1.1}$$

where Δt is the time step in seconds, $R = 2$ for $T \geq 43$ °C, and $R = 4$ for $T < 43$ °C (Sapareto et al., 1984). Thermal dose is the length in minutes of an equivalent treatment at 43 °C. Figure 1.1 indicates thermal dose thresholds for treated ($\mathrm{EM}_{43} = 200$ min) and ablated tissue ($\mathrm{EM}_{43} = 10^7$ min) (Mast et al., 2005). In one second, the treated threshold is achieved at 56 °C and the ablated threshold is achieved at 72 °C. In 60 minutes, the treated threshold is achieved at 45 °C and the ablated threshold is achieved at 60 °C. These thermal dose thresholds are consistent with empirical tissue viability studies (Karunakaran et al., 2012). The typical cell–death pathway undergone by thermally ablated cells is coagulative necrosis

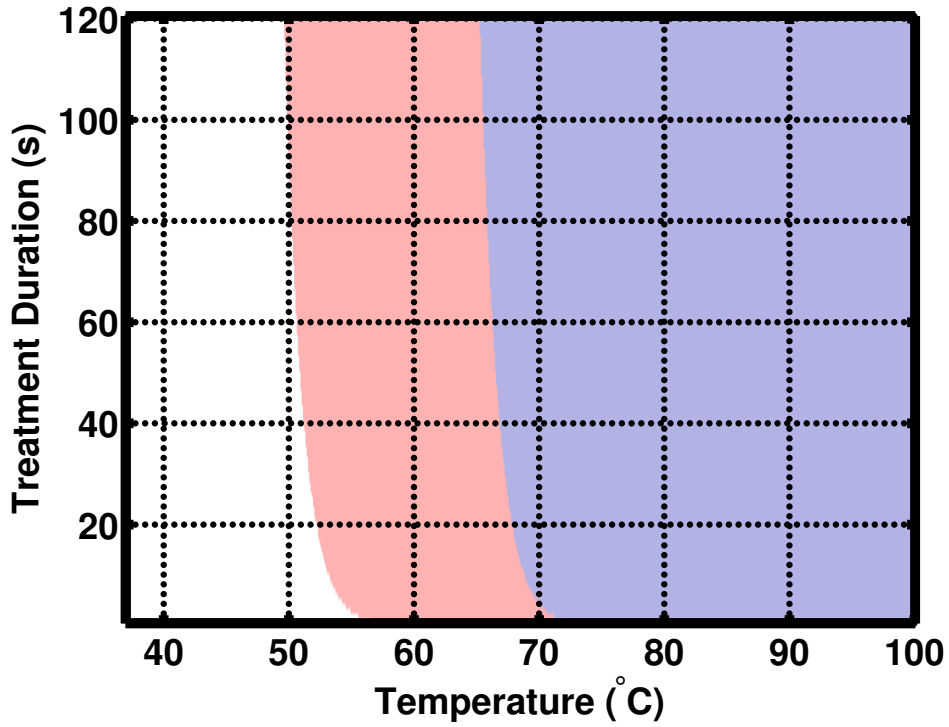

Figure 1.1: Local thermal dose is a function of temperature and treatment duration. The white region indicates healthy tissue, the red region indicates treated tissue (EM_{43} = 200 min.) and the purple region indicates ablated tissue ($EM_{43} = 10^7$ min.) (Sapareto et al., 1984; Mast et al., 2005; Karunakaran et al., 2012)

.

(Goldberg, 2001). Thermal ablation approaches aim to achieve and maintain temperatures between 50–100 °C as temperatures greater than 100 °C result in poor therapy delivery due to processes including tissue boiling, vaporization, and carbonization (Goldberg, 2001).

1.1.2.1 Radiofrequency ablation

Radiofrequency ablation (RFA) is the standard minimally invasive liver cancer treatment approach that uses radiofrequency (< 1 MHz) energy to achieve cytotoxic effects (Goldberg, 2001; Nishikawa et al., 2013; Li et al., 2014). RFA is sometimes used in tandem with transarterial chemoembolizatoin (TACE) to reduce perfusion effects which can lead to incomplete thermal lesioning, resulting in tumor recurrence (Bruix et al., 2005; Li et al., 2014). There is a

wide spectrum of RFA technologies including monopolar and bipolar electrodes deployed for liver cancer thermal ablation (Goldberg, 2001). Monopolar electrodes are capable of achieving spheroidal thermal lesions up to 1.6 cm diameter in approximately 6 minutes (Goldberg, 2001). In monopolar mode, a surface grounding pad completes the electric circuit (Brace et al., 2009). In bipolar mode, grounding electrodes replace the grounding pad (Brace et al., 2009; Li et al., 2014). In bipolar configurations, additional heating is achieved at the grounding electrode site resulting in larger lesion long–axis dimensions (e.g., 4.0 cm) but smaller short–axis dimensions (e.g, 1.4 cm) (Goldberg, 2001). Monopolar configurations are more frequently deployed (Brace et al., 2009). To achieve larger ablation volumes, multiprobe, cluster and internally–cooled electrodes have been developed (Goldberg, 2001). Pereira et al. (2004) observed larger lesioning for internally cooled cluster devices. More spherical and reproducible lesions were obtained with multiprobe arrays (Pereira et al., 2004). Pereira et al. (2004) suggested that the reproducibility seen for the multiprobe arrays might suggest improved lesion dimension predictability. Typical RFA tip temperatures range between 70 and 90 °C (Goldberg, 2001).

1.1.2.2 Microwave ablation

Microwave ablation is a minimally invasive hyperthermic approach that leverages microwave radiation (900 to 2450 MHz) to achieve cytotoxic effects (Simon et al., 2005). The use of microwave ablation for liver tumors has increased and demonstrated equivalent clinical efficacy compared to radiofrequency ablation (RFA) (Li et al., 2014). In principle, the benefits of microwave ablation in comparison to RFA include: larger ablation volumes, faster ablation times, and less susceptibility to perfusion effects. These benefits are due to the faster heating rates and improved power vs. heating linearity (Brace et al., 2009; Li et al., 2014). Microwave ablation systems can be much simpler as they do not require grounding pads like RFA (Simon et al., 2005; Li et al., 2014).

1.1.2.3 Ultrasound ablation

High–intensity focused ultrasound (HIFU) is a thermal ablation approach which enables non–invasive transcutaneous treatment (Maruyama et al., 2008). Ultrasound is focused to a specified treatment volume and the acoustic energy is converted into heat resulting in thermal–induced necrosis in the focal area with less damage to the surrounding tissue (Kennedy et al., 2003). The temperature at the focus can rise rapidly above 80 °C (Kennedy et al., 2003). Transcutaneous HIFU approaches also avoid needle track seeding (Aubry et al., 2013). Oncological HIFU applications approved outside the United States are for bone metastases, liver tumors, pancreatic tumors, prostate cancer, kidney tumors, and breast cancer [Figure 1.2, (Focused Ultrasound Foundation, 2015)]. FDA approved HIFU applications are for bone metastases and uterine fibroids (Focused Ultrasound Foundation, 2015). However, shadowing effects of the ribs, breathing motion, and relatively long treatment times (i.e., 1 hour treatment for a superficial 2 cm tumor) are current barriers to clinical adoption (Aubry et al., 2013; Kennedy et al., 2003). Initial studies have investigated the safety and efficacy of HIFU and demonstrated its potential as a local ablative approach (Li et al., 2014).

Bulk ultrasound ablation utilizing interstitial probes or catheter–based devices with cylindrically omnidirectional (Diederich et al., 1999), planar (Mast et al., 2005), and weakly focused (Lafon et al., 2002) transducer configurations have also been developed for tumor ablation. Bulk ultrasound approaches are capable of ablating larger tissue volumes in comparison to HIFU within treatment durations similar to RFA (Makin et al., 2005). However, this approach is sensitive to perfusion heat sink effects, increasing the risk of incomplete treatment (Mast et al., 2005). Both HIFU and bulk ultrasound approaches offer improved spatial selectivity and monitoring in comparison to RFA and microwave ablation (Makin et al., 2005). This treatment enhancement is achieved by image–ablate or dual–mode arrangements which allow coplanar imaging and ablation (Makin et al., 2005).

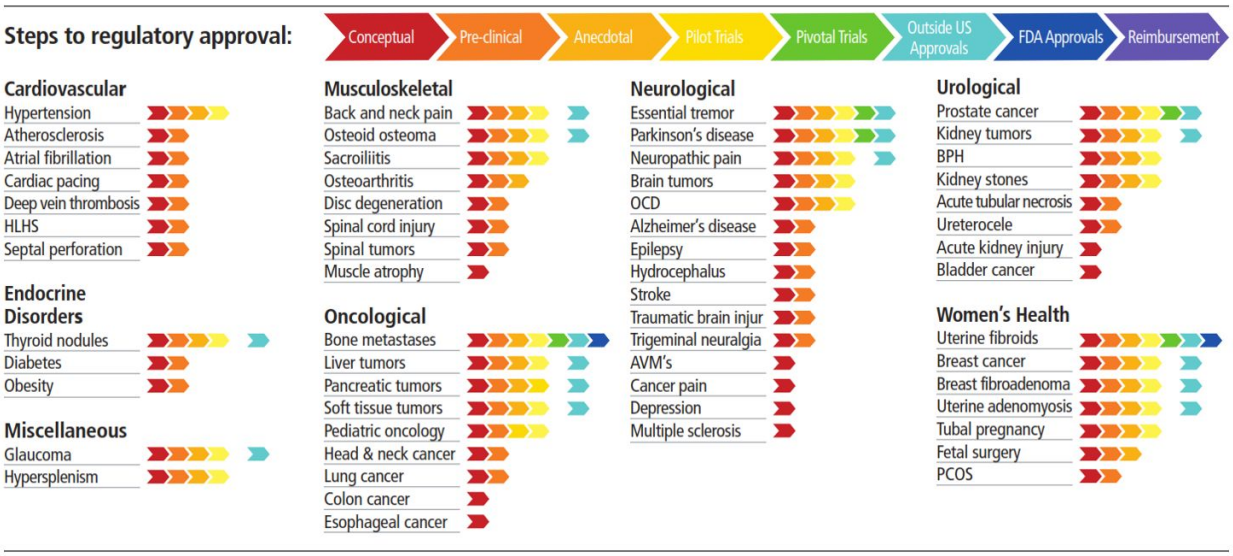

Figure 1.2: The number of clinical applications of HIFU being researched, developed, and commercialized is growing and indicates HIFU's importance in disease treatment (Focused Ultrasound Foundation, 2015).

1.1.3 Clinical needs: thermal ablation monitoring

Mulier et al. (2005) reported local tumor recurrence rates between 2% and 60% for 5,224 RFA procedures performed worldwide between 1990 and 2004. Analysis by Mulier et al. (2005) indicated larger tumor size and increased heat sink effects (i.e., perfusion) as factors associated with higher local recurrence rates.

Radiofrequency ablation (RFA) and similar approaches (i.e., HIFU and bulk ultrasound ablation) would be improved if used concurrently with a suitable real time monitoring method allowing local heat–induced cell death visualization (Li et al., 2014). Tissue temperature effects can be monitored by magnetic resonance thermometry; however, these clinical extracorporeal systems [e.g., ExAblate, InSightec Inc., Tirat Carmel, Israel (Kennedy et al., 2003)] can be costly and cumbersome (Napoli et al., 2013). In China, a clinical extracorporeal ultrasound–guided focused ultrasound (USgFUS) system has demonstrated liver tumor treatment efficacy and safety [(Wu et al., 2009), Chongqing HAIFU, Technology Company,

Chongqing, P.R., China]. Other USgFUS systems are the Sonablate (Focal Surgery, Milpitas, CA, US) and the Ablatherm (Technomed International, Lyon, France) which are used to treat prostate cancer (Kennedy et al., 2003). Both the Sonablate and Ablatherm systems measure echo energy (e.g., integrated backscatter), possibly due to acoustic cavitation, to provide treatment feedback (Chen, W. H.; ter Haar et al., 2007). Inconsistent echogenicity changes (Mast et al., 2008) or pulse–echo signal decorrelation (Cespedes et al., 1997) can render current ultrasound monitoring approaches, including conventional B–mode (brightness mode) imaging (Maruyama et al., 2008), echo energy–based methods [e.g., attenuation and integrated backscatter (Zhang et al., 2009)], and cross–correlation–based methods [e.g., echo strain (Liu et al., 2010) and elastography (Kolokythas et al., 2008) imaging], unreliable or limited in application.

1.1.4 Ultrasound echo decorrelation imaging

Ultrasound echo decorrelation, a pulse–echo method that maps heat–induced changes in ultrasound echoes over millisecond time scales, shows promise for real time radiofrequency and ultrasound thermal ablation guidance and monitoring (Mast et al., 2008; Subramanian et al., 2014; Fosnight et al., 2014). However, echo decorrelation's ability to predict the desired clinical end effect (i.e., death of malignant tumor tissue) in a living subject, where motion could limit echo decorrelation's performance, has not been investigated. Tissue structural changes, pulse–echo strain, vaporization and dissolution of gas as a result of thermal–induced coagulative necrosis could cause echo decorrelation during thermal ablation (Hooi et al., 2015). Additionally, acoustic cavitation could cause echo decorrelation during ultrasound thermal ablation.

Subramanian et al. (2014) investigated echo decorrelation's ability to predict *in vivo* bulk ultrasound ablation of VX2 tumor and surrounding liver tissue and prediction performance of *in vivo* RFA of porcine liver. However, poor resolution pulse–echo images could not confirm

a direct link between echo decorrelation and ultrasound ablated VX2 tumor. The ability of echo decorrelation imaging to predict *in vivo* HIFU ablation was also not investigated.

Subramanian et al. (2014) reduced motion–induced artifacts using motion gating; however, a more effective motion compensation method has employed a theory separating decorrelation caused by motion, electronic noise, and heat–induced tissue changes, allowing compensation for estimated or measured artifactual decorrelation (Hooi et al., 2015). This compensation method was shown to allow accurate reconstruction of scattering medium decoherence in image simulations and to substantially reduce motion–induced decorrelation artifacts during *in vivo* RFA (Hooi et al., 2015).

1.1.4.1 Theory

Corrected echo decorrelation and integrated backscatter images (IBS) were previously described by Hooi et al. (2015). Briefly, local echo decorrelation per unit time is defined as

$$\Delta_{\text{local}}(y,z,t) = 2\frac{\beta^2 - |R_{01}(y,z,t)|^2}{\tau[\beta^2(y,z,t) + \overline{\beta(t)^2}]}, \tag{1.2}$$

where y is the azimuthal (array) coordinate, z is the range (depth) coordinate, and τ is the inter–frame time in milliseconds. R_{01} is the position–dependent, zero–lag, windowed spatial cross–correlation between two sequential complex image frames $I(y,z,t)$ and $I(y,z,t+\tau)$ separated in time by τ:

$$\begin{aligned} R_{01}(y,z) &= \iint w(y-y',z-z')I(y,z,t)^* I(y,z,t+\tau)dy'dz' \\ &= \langle |I(y,z,t)^* I(y,z,t+\tau)| \rangle. \end{aligned} \tag{1.3}$$

The star indicates complex conjugation and the angle brackets denote a convolution with the window function. The window function $w(y,z)$, is a two–dimensional isotropic spatial

Gaussian filter with width parameter σ:

$$w(y,z) = e^{-\frac{y^2+z^2}{2\sigma^2}}. \tag{1.4}$$

An integrated backscatter term $\beta(y,z,t)$ is then defined as:

$$\beta(y,z,t) = \sqrt{R_{00}(y,z,t)R_{11}(y,z,t)} \tag{1.5}$$

and $\overline{\beta(t)}$ is the spatial average of the integrated backscatter term. R_{00} and R_{11} are the corresponding zero–lag image autocorrelations:

$$R_{00}(y,z) = \langle |I(y,z,t)|^2 \rangle \text{ and } R_{11}(y,z) = \langle |I(y,z,t+\tau)|^2 \rangle. \tag{1.6}$$

As echo decorrelation varies stochastically during ablation, temporal averaging is used to provide a better estimate of local tissue changes. The temporal maximum of the averaged Δ_{local} at each tissue position is referred to as the cumulative echo decorrelation and is hypothesized to predict local heat–induced cell death during ablation.

Estimates of artifactual cumulative echo decorrelation obtained from corresponding sham trials denoted Δ_{sham} are used to construct corrected cumulative echo decorrelation, denoted $\Delta_{\text{corrected}}(y,z,t)$, from uncorrected cumulative echo decorrelation denoted $\Delta_{\text{uncorrected}}$ using the equation (Hooi et al., 2015):

$$\Delta_{\text{corrected}}(y,z,t) = \frac{\Delta_{\text{uncorrected}} - \Delta_{\text{sham}}}{1 - \Delta_{\text{sham}}}. \tag{1.7}$$

Relative integrated backscatter (IBS) images are defined as the decibel–scaled ratio between $\beta(y,z,t)$ during ablation and the cumulative integrated backscatter $\beta_{\text{sham}}(y,z)$ mea-

sured for the corresponding sham trial:

$$\mathrm{IBS}(y,z,t) = 10 \cdot \log_{10}\left(\frac{\beta(y,z,t)}{\beta_{\mathrm{sham}}(y,z)}\right), \tag{1.8}$$

where β is the integrated backscatter function defined by Equation (1.5). The cumulative relative integrated backscatter map is the temporal maximum of $\mathrm{IBS}(y,z,t)$.

1.1.4.2 Preliminary *in vitro* ultrasound ablation results

Preliminary bulk ultrasound and HIFU thermal ablation experiments using *in vitro* bovine liver (Fosnight et al., 2014) deploying noise correction (Hooi et al., 2015) showed significant ablation prediction by echo decorrelation.

Ablation and imaging were performed using custom 64 element, 5×24 mm^2 linear image–ablate arrays with >40% pulse–echo fractional bandwidth for imaging and >40 W available acoustic power for therapy, controlled by the Iris 2 ultrasound imaging and therapy system [Ardent Sound Mesa, AZ, USA; Barthe et al. (2004)].

For these *in vitro* experiments, pulse–echo images were acquired for both focused ultrasound ablation (N=21, 1 s sonications, 17% duty factor, 6 sonication pulses, 284–769 W/cm^2 *in situ* spatial-peak, temporal-peak intensity [I_{sptp}], electronically focused 10 mm into the tissue) and bulk ultrasound ablation (N=12, 7.5 s sonications, 60% duty factor, 6 sonication pulses, 50.9–101.8 W/cm^2 *in situ* [I_{sptp}], unfocused aperture). The beamformed, radiofrequency echo signals were captured at 118 frames per second during 5.0 s rest periods for both ablation trials and matching sham trials, beginning 1.1 s after each sonication pulse, using a 14–bit, PC-based A/D converter at 33.3 MHz (CompuScope CS 14200, Gage Applied Technologies, Montreal, QC, Canada). Echo decorrelation and IBS images were computed using Equations 1.2–1.6 and a temporal running average was used to provide a

lower-variance estimate of local tissue changes (Fosnight et al., 2014):

$$\overline{\Delta}_{\text{uncorrected}}(y,z,t) = (1-\epsilon)\overline{\Delta}_{\text{uncorrected}}(y,z,t-\tau) + \epsilon\Delta_{\text{uncorrected}}(y,z,t), \tag{1.9}$$

where the averaging parameter $\epsilon = 0.05$. The temporal maximum of the running-average echo decorrelation and IBS at each tissue location are referred to as the cumulative echo decorrelation and IBS images. To remove artifactual decorrelation caused by electronic noise and tissue or array motion, Equation 1.7 was used.

Tissue samples were frozen at −80 °C, sectioned, vitally stained, imaged, and semi-automatically segmented for receiver operating characteristic (ROC) analysis. ROC curves were constructed and the area underneath the curve (AUC) computed to assess prediction performance for echo decorrelation and IBS. Logarithmically scaled echo decorrelation in non-ablated and ablated tissue regions before and after electronic noise and motion correction were compared.

Representative $\log_{10}$–scaled echo decorrelation, decibel–scaled integrated backscatter (IBS), and corresponding triphenyl tetrazolium chloride (TTC) stained tissue histology images are shown in Figure 1.3. In general, good correspondence between echo decorrelation maps and tissue histology (Figure 1.3 B and E) was seen in comparison to IBS maps (Figure 1.3 A and D).

Mean and standard error values of the $\log_{10}$-scaled mean echo decorrelation within ablated tissue regions and non-ablated tissue regions for the 12 unfocused exposures, the 15 focused exposures, and the combined 27 exposures producing a thermal lesion are shown in Figure 1.4 A–C. The $\log_{10}$–scaled mean echo decorrelation within ablated regions was significantly greater than in non–ablated regions for unfocused exposures (mean±standard error -3.82 ± 0.26 ablated; -4.15 ± 0.26 non–ablated; t=1.70, p=5.83±10^{-2}, N=12), for focused exposures (-4.37 ± 0.18 ablated; -4.63 ± 0.13 non–ablated; t=2.45, p=2.58·10^{-2}, N=15),

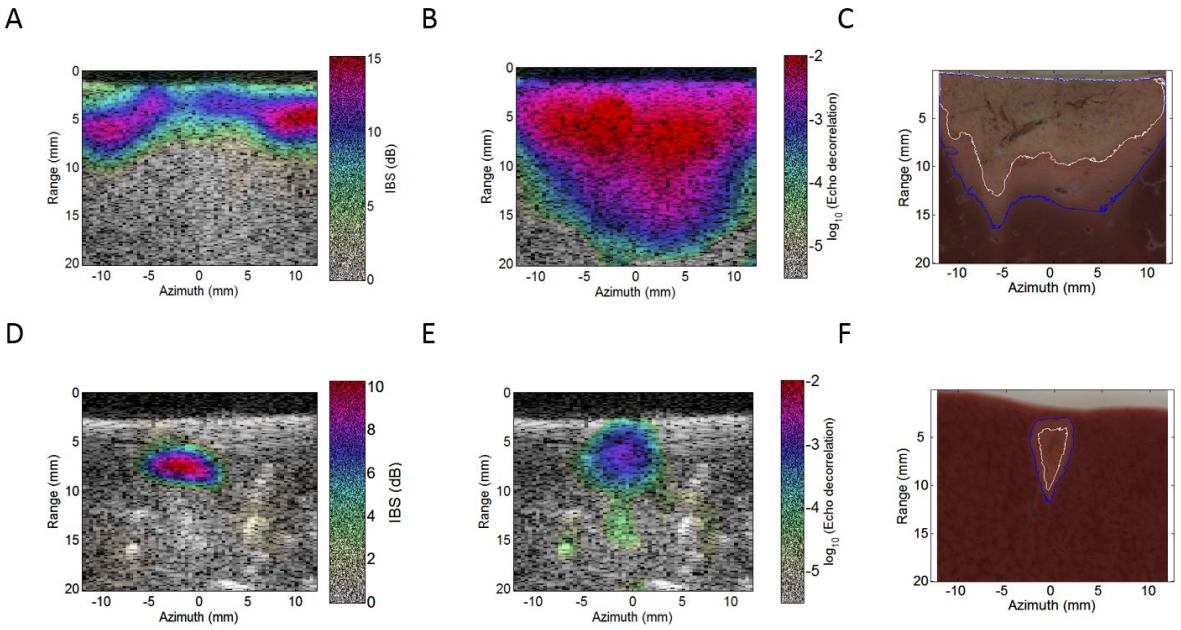

Figure 1.3: Representative IBS (A and D), echo decorrelation (B and E), and segmented triphenyl tetrazolium chloride (TTC) stained tissue histology (C and F) images for bulk ultrasound (top row) and HIFU (bottom row) ablation. In the TTC–stained tissue sections, the outer blue boundary indicates the margin of incomplete ablation (TTC uptake in blanched tissue regions) while the inner white boundary indicates the margin of completed ablation (no TTC uptake).

and for all exposures combined (-4.13 ± 0.16 ablated; -4.42 ± 0.14 non–ablated; t=2.71, p=$5.92\cdot10^{-3}$, N=27). The $\log_{10}$–scaled echo decorrelation within non–ablated regions was significantly reduced by correction for noise and motion (t=-7.45, p=$3.29\cdot10^{-8}$, N=27).

Corresponding ROC curves for each group of experiments are shown in Figure 1.4 D–F. Local ablation was predicted significantly better than chance by both echo decorrelation and IBS for the 12 unfocused exposures (echo decorrelation AUC=0.58, p =$3.12\cdot10^{-4}$; IBS AUC=0.60, p=$1.11\cdot10^{-5}$), for the 21 focused exposures (echo decorrelation AUC=0.69, p=$4.74\cdot10^{-5}$; IBS AUC=0.64, p=$3.10\cdot10^{-3}$), and for the combination of all 33 exposures (echo decorrelation AUC=0.69, p=$1.00\cdot10^{-12}$; IBS AUC=0.60, p=$2.02\cdot10^{-7}$). For the ROC curves computed from all 33 trials, the AUC for echo decorrelation was significantly greater for than for IBS (p=$1.76\cdot10^{-7}$).

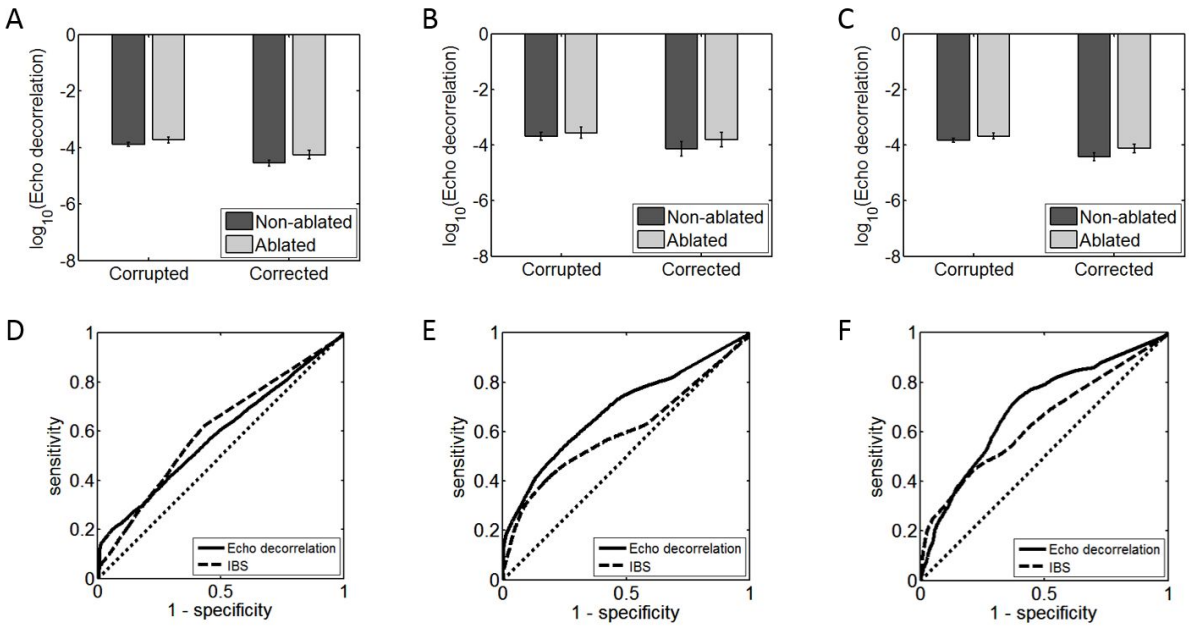

Figure 1.4: Mean and standard error of $\log_{10}$–scaled uncorrected and corrected echo decorrelation in non–ablated and ablated regions for *ex vivo* bulk ultrasound (A), HIFU (B), and combined bulk ultrasound and HIFU (C) ablations; ROC curves for bulk ultrasound (D), HIFU (E), and combined bulk ultrasound and HIFU (F) ablations.

These preliminary *in vitro* results indicate that echo decorrelation imaging is a successful predictor of local ablation. Consistent with previous studies, ablation prediction by echo decorrelation was more successful than prediction by integrated backscatter (Mast et al., 2008; Subramanian et al., 2014). Real–time monitoring by echo decorrelation imaging is thus a promising approach for real time prediction of heat–induced cell death during clinical thermal ablation treatments, including minimally invasive radiofrequency and HIFU ablation. Optimization of imaging parameters, including decreasing the time between sonication and imaging cycles and optimizing the pulse–echo image frame rate, and optimal threshold design for treatment control may further improve tissue ablation prediction performance, increasing the utility of echo decorrelation for treatment monitoring.

1.2 Research hypotheses and specific aims

Our overall research objective is to provide clinicians with a real time, ultrasound–based imaging approach to predict thermal–induced cell death during thermal ablation. The **central hypothesis** of this study is that ultrasound echo decorrelation accurately predicts *in vivo* ultrasound thermal ablation. To test this hypothesis the following specific aims were completed:

1.2.1 Specific aim 1: Test ultrasound echo decorrelation's cell–death prediction performance

In vivo pulse–echo imaging of HIFU and bulk ultrasound thermal ablation were performed on rabbit liver parenchyma and VX2 tumor. Ablation and imaging were performed using the same image–ablate arrays, allowing precise comparison of image results and ablated tissue histology. The prediction performance of echo decorrelation before and after motion compensation was assessed by quantitatively comparing it with triphenyl tetrazolium chloride (TTC) stained gross histology and then computing its receiver operating characteristic (ROC) curves. For comparison, the decibel–scaled integrated backscatter (IBS) and ROC curves were also computed.

1.2.2 Specific aim 2: Establish design criteria for successful clinical translation of cell–death prediction by echo decorrelation

To achieve real time thermal ablation guidance and monitoring, the effects of a realistic clinical setting must be understood. Additionally, echo decorrelation thresholds which indicate the desired clinical end effect must be established. In this study, optimal thresholds for echo decorrelation monitoring and control of HIFU and bulk thermal ablation of normal liver and VX2 tumor were determined. The effects of artifactual echo decorrelation due to *in vivo*

tissue motion were also assessed by increasing the inter–frame time for echo decorrelation computation. These parameters will aid system and ablation control algorithm design for future clinical thermal ablation experiments.

Chapter II

Motion–Corrected Echo Decorrelation Imaging of *In Vivo* HIFU and Bulk Ultrasound Ablation in Rabbit Liver and VX2 Tumor

2.1 Introduction

The ability of echo decorrelation imaging to accurately predict local heat–induced cell death in rabbit liver and VX2 tumor tissue was tested using pulse–echo ultrasound data recorded during *in vivo* high–intensity focused ultrasound (HIFU) and bulk ultrasound thermal ablation experiments. The effect of tissue movement on echo decorrelation ablation prediction was investigated and optimal thresholds for ablation prediction were determined. Materials and methods used for the experiments, image formation, and data analysis are described below. All animal experiments were performed according to protocols approved by the University of Cincinnati Institutional Animal Care and Use Committee (IACUC).

2.2 Materials and methods

2.2.1 VX2 tumor model

The VX2 tumor used for this study has been widely used for liver tumor therapy research as it easily grows in rabbit liver and develops into discrete lesions (Wu et al., 2009). Viable VX2 tumor fragments were implanted in each of the three main liver lobes of New Zealand white rabbits and allowed to grow for two weeks (Figure 2.1). Thirty–eight tumors successfully grew out of the 42 implanted tumor fragments. Gross tumor images within the pulse–echo imaging plane were assessed. For the tissue sections facing one another, effective tumor diameters [i.e., diameters of circles with area equal to measured tumor areas (Mast et al., 2011)] were computed and the maximum of these two effective diameters was recorded. Tumor diameters were 8.4 ± 3.3 mm for two weeks growth (N=23). Of these 23 tumors, the 14 used for *in vivo* ablation trials described below measured 7.9 ± 3.5 mm in diameter (Appendix Table 4.2).

2.2.2 Thermal ablation experiments

Ablation and imaging were performed using custom 64 element, 5×24 mm^2 linear image–ablate arrays with >40% pulse–echo fractional bandwidth for imaging and >40 W available acoustic power for therapy, controlled by the Iris 2 ultrasound imaging and therapy system [Ardent Sound Mesa, AZ, USA; Barthe et al. (2004)]. Pulse–echo imaging was performed with a single transmit focal depth (3.5 cm, F–number=4).

The setup for these *in vivo* experiments is shown in Figure 2.1. In procedures performed on 11 animals, the animal was anesthetized and its liver was exposed. The tumor was located visually on the surface of the liver and indelible marks were made on the surface to guide probe placement onto the tumor. Alignment with the tumor was verified by visualizing the tumor in the B–mode (brightness mode) image. The array aperture was placed parallel

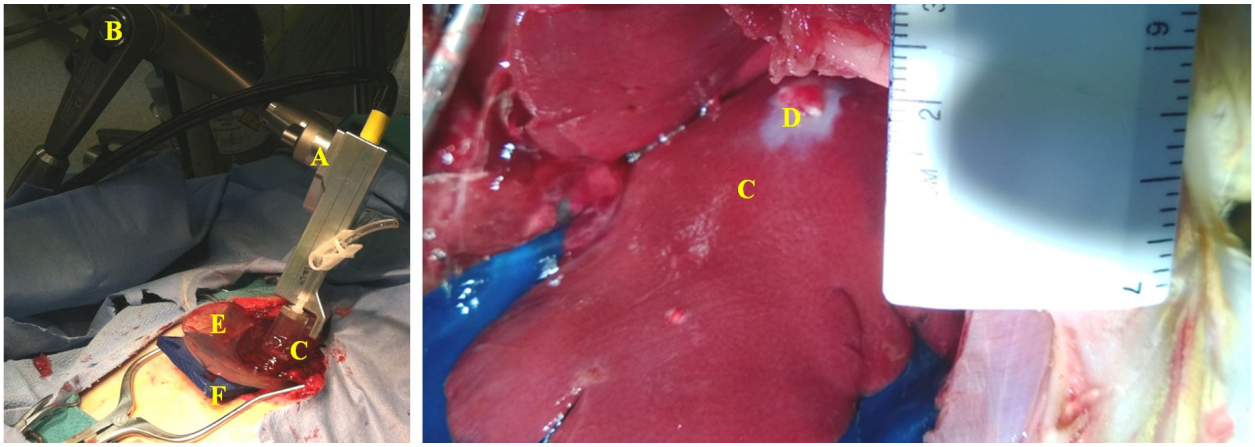

Figure 2.1: Experimental setup for focused and unfocused ultrasound exposures of *in vivo* rabbit liver. Image–ablate arrays (A) were held by a three–dimensional positioning arm (B). The liver lobe (C) with implanted VX2 tumor (D) was placed on an acoustic gel coupling pad (E) and/or acoustic absorber pad (F) before performing imaging and thermal ablation.

to the liver capsule surface at a distance of 23 mm using a water–filled standoff with an acoustically transparent membrane window (Tegaderm, 3M, St Paul, MN, USA). Coupling of the membrane to the tissue was achieved with an acoustic transmission gel (LithoClear, Next Medical Products, Bellingham, WA, USA). To achieve accurate registration between tissue histology and ultrasound images, the probe was fixed by a three–dimensional positioning arm (Atlas Multifunctional Arm, Medical Intelligence, Schwabmünchen, Germany) to minimally compress the liver. A gel acoustic coupling pad (Aquaflex, Fairfield, NJ, USA) or rubber acoustic absorber pad (Aptflex F28, Precision Acoustics Ltd., Dorchester, Dorset, UK) were placed underneath the liver tissue to limit heating from reflections at the tissue–absorber boundary and to constrain the liver lobe's shape, allowing accurate registration of tissue viability and parameter maps.

Thermal lesions were formed in VX2 tumor and liver regions using continuous–wave sonications with center frequency f_c = 5.00, 5.05, 5.20, or 5.40 MHz (Appendix Table 4.1). For bulk ablation (N=10), a 64–element aperture fired pulses of 50–63 W/cm^2 *in situ* spatial–peak, temporal–peak intensity (I_{sptp}) for 7–9 sonication pulses, totaling 76.5 s total ablation

time (71% duty cycle). For HIFU ablation (N=13), a 64–element aperture electronically focused at a single focal point 2 mm into the tissue fired 6–9 pulses with 911–1351 W/cm^2 *in situ* I_{sptp} (spatial–peak, temporal–peak intensity), resulting in 31.5 s total ablation time (20% duty cycle). The *in situ* I_{sptp} was computed from simulated acoustic fields of the linear image–ablated array using methods described by Mast et al. (2007). Representative simulations for focused and unfocused exposures are illustrated in Figure 2.2.

To assure that viability maps in the image–treat plane could be obtained for HIFU ablation experiments, two thermal lesions used as registration marks were formed by firing unfocused sub–apertures comprising elements, 1–10, and then elements 55–64. Each sub–aperture fired pulses of 59 W/cm^2 until a visible lesion was seen on the liver surface. Registration mark formation was confirmed by simulation (Mast et al., 2005) not to elevate temperature at the focus position above 2 °C.

After each sonication pulse, 114 frames of beamformed, radiofrequency echo signals were captured at a rate of 118 frames per second, beginning <10 ms or <1.1 s after each sonication pulse, using a PC–based data acquisition system with a 33 MHz sampling rate (CompuScope CS 14200, Gage Applied Technologies, Montreal, QC, Canada).

2.2.3 Image processing

Before further processing, echo signals were demodulated with a 5.0 MHz center frequency and decimated to in–phase and quadrature (IQ) components with a sampling rate of 5.56 MHz. This data acquisition was performed both for ablation trials and for matching sham trials, used for estimation and correction of decorrelation artifacts.

The IQ echo signals were processed to construct integrated backscatter (IBS) and decorrelation per millisecond (referred to as echo decorrelation in this thesis) images using Equations 1.2–1.8 found in Chapter 1. Tissue boundaries were manually segmented in the ultrasound images to eliminate echoes from outside the liver lobe. Echo decorrelation and IBS were

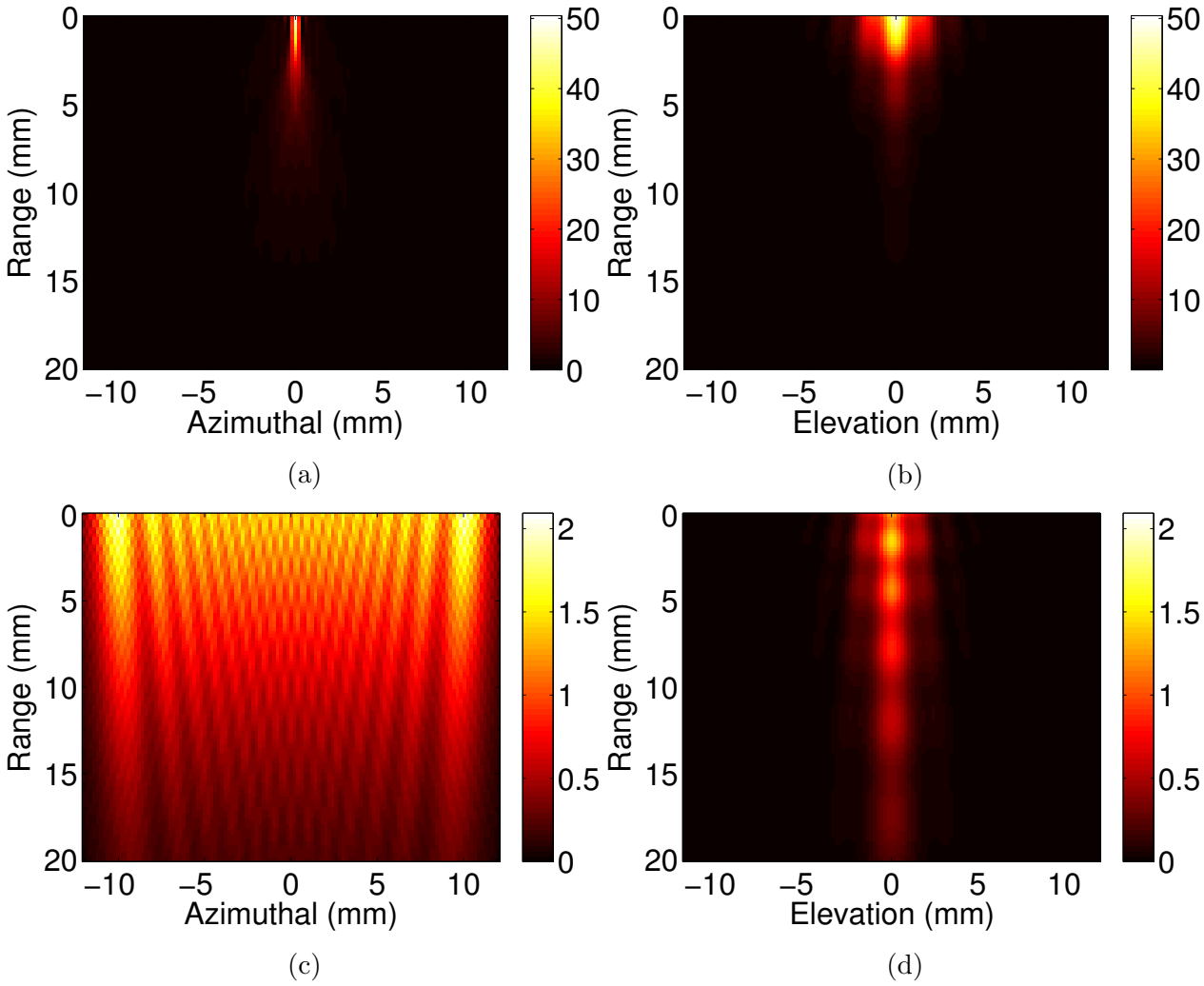

Figure 2.2: Simulated intensity beams for the focused (2.2a and 2.2b; electronically focused to 25 mm) and unfocused (2.2c and 2.2d; electronically focused to ∞) linear–array apertures deployed for these *in vivo* experiments. The beams were simulated for the field just beyond the 22 mm standoff.

calculated within the segmented tissue boundaries as seen in the ultrasound images. The Gaussian window function (Equation 1.3) width parameter (σ) for decorrelation and IBS calculation was 1.0 mm.

The local instantaneous decorrelation was averaged over each frame group (i.e., ensemble averaged) containing 112 frames taken after each sonication cycle (Figure 2.3). The cumulative decorrelation was defined as the temporal maximum of the ensemble–averaged Δ_{local}.

Estimates of artifactual cumulative decorrelation obtained from corresponding sham trials, denoted Δ_{sham}, were used to construct corrected cumulative decorrelation, denoted $\Delta_{\text{corrected}}(y, z, t)$, from uncorrected cumulative decorrelation, denoted $\Delta_{\text{uncorrected}}$, using Equation 1.7. This correction was only applied at locations where $\Delta_{\text{uncorrected}}$ exceeded a dynamically set threshold defined as 10 times the minimum of the corresponding Δ_{sham}. At locations where Equation 1.7 would result in corrected values less than zero, $\Delta_{\text{corrected}}$ was set equal to the minimum value of Δ_{sham}.

B–mode images were constructed from the $\log_{10}$–scaled envelopes ($|p(y, z, t)|$) of the IQ data and displayed on a 60 dB dynamic range. Hybrid B–mode/decorrelation and B–mode/IBS images were constructed by overlaying the B–mode and $\log_{10}$–scale decorrelation images and decibel–scaled IBS images (Mast et al., 2008). All image processing was performed in MATLAB (The MathWorks, Natick, MA, USA).

2.2.4 Analysis of imaging delay effects

Post sonication temperature decay effects on echo decorrelation measurements were investigated because relatively high local echo decorrelation decay rates were observed after focused sonication (Figure 2.3a). An analytic solution to the homogeneous bio–heat transfer equation without perfusion was used to estimate these temperature decay effects. Green's functions were used to solve the bio–heat transfer equation without perfusion analytically

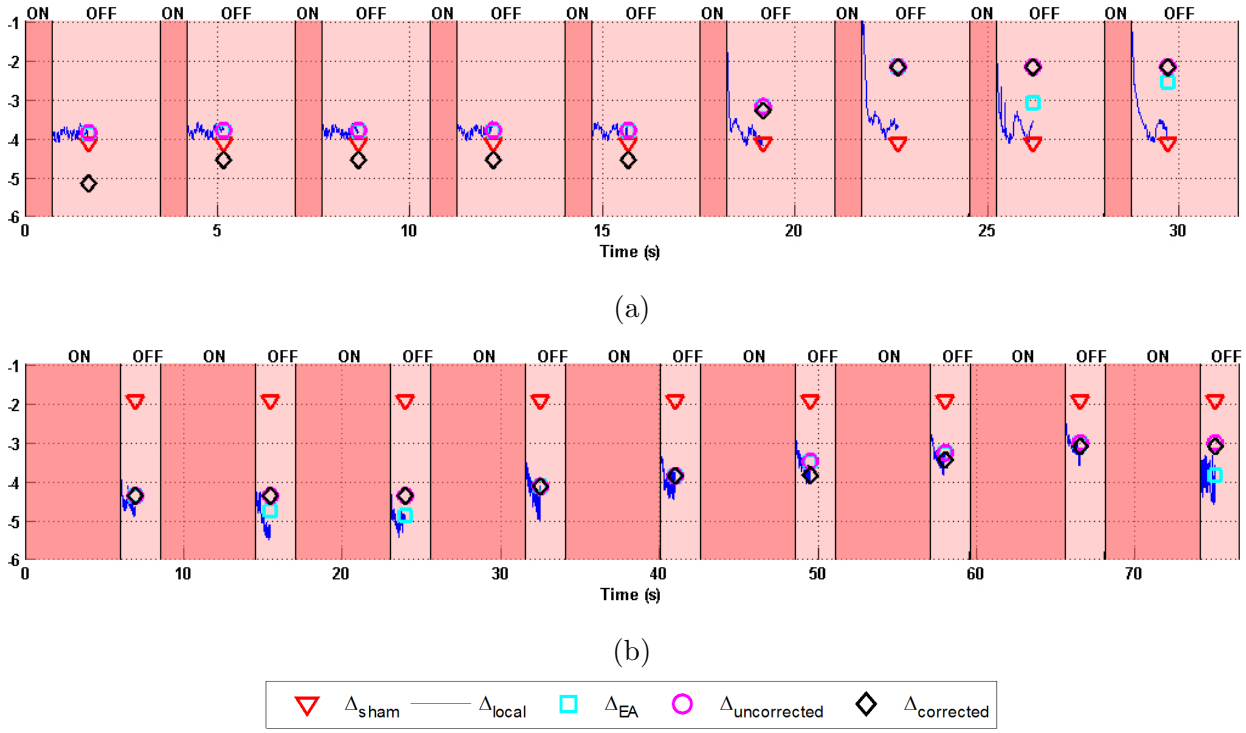

Figure 2.3: Representative echo decorrelation time history at a local echo decorrelation maximum: cumulative sham (Δ_{sham}) and instantaneous (Δ_{local}), ensemble-averaged (Δ_{EA}), uncorrected cumulative ($\Delta_{\text{uncorrected}}$), and corrected cumulative ($\Delta_{\text{corrected}}$) echo decorrelation values for *in vivo* HIFU (2.3a) and bulk (2.3b) ultrasound thermal ablation. Tissue was sonicated (ON) 0.7 s for HIFU and 6–7.5 s for bulk thermal ablation. Echo decorrelation was calculated from ultrasound pulse–echo images acquired during 2.8–3.3 s rest periods (OFF) for HIFU and 2.5–5 s for bulk thermal ablation.

(Ozisik et al., 1993):

$$\frac{\partial T(\vec{r},t)}{\partial t} = K\nabla^2 T(\vec{r},t), \tag{2.1}$$

where $T(\vec{r},t)$ is the spatio–temporal temperature elevation profile, r is the magnitude of the position vector $\vec{r}$, and K is the thermal diffusivity of liver tissue. Assuming radial symmetry, the Green's function for this system in spherical coordinates is (Ozisik et al., 1993)

$$G(\vec{r}) = \frac{e^{-r^2/(4Kt)}}{8\pi^{3/2}(Kt)^{3/2}}. \tag{2.2}$$

The initial temperature condition was proportional to the intensity beam of the acoustic source. An approximate representation of this heating pattern was assumed sufficient for an order–of–magnitude estimate of the imaging delay effects. To this end, a Gaussian distribution was used for the initial condition:

$$T_i(\vec{r}) = T_0 e^{-\frac{r^2}{2\sigma^2}}, \tag{2.3}$$

where the Gaussian width parameter σ was set equal to 10 mm for unfocused ablation and 0.1 mm for focused ablation. These widths were estimated by minimizing the mean–squared error between a Gaussian and simulated transverse beam profiles containing the spatial peak–temporal peak intensity (Figures 2.4a and 2.4c). The beam profiles were obtained from simulated acoustic fields of the unfocused (focal depth = ∞) and focused (focal depth = 25 mm) linear image–ablate array (Mast et al., 2007). The analytic solution for the temperature profile post sonication follows as

$$T(\vec{r},t) = \int_{V_0} G(\vec{r}-\vec{r_0},t)T_i(\vec{r_0})dV_0 = T_0\frac{\sigma^3 e^{-\frac{r^2}{4Kt+2\sigma^2}}}{(2Kt+\sigma^2)^{3/2}}, \tag{2.4}$$

where the thermal diffusivity of liver tissue was $K = 0.137$ (mm^2/s) (Mast et al., 2005). The estimated maximum temperature decrease during the <10 ms delay was 20% and < 0.1% for the focused and unfocused trials. The estimated maximum temperature decrease during the 1.1 s delay was > 90% and 0.5% for the focused and unfocused trials. For these reasons, the focused trials with a 1.1 s delay were removed from this study.

2.2.5 Tissue processing

After ablation, the animal was euthanized. The liver lobes were removed and sectioned parallel to the image–ablate plane with a scalpel. Sectioning was performed within 2 hours post–ablation. The surface closest to the image–ablate plane was stained with a 2% (w/v) solution of triphenyl tetrazolium chloride (TTC; Sigma–Aldrich, St. Louis, MO, USA) in 0.1 M phosphate–buffered saline (Sigma–Aldrich, St. Louis, MO, USA) for 20 minutes with the image–ablate plane face down in the TTC well. TTC uptake indicates metabolically active tissue, while no TTC uptake indicates inactive tissue (Scheffer et al., 2014).

Tissue images were manually segmented to delineate boundaries of the liver lobes, VX2 tumors, regions of reduced TTC stain uptake, and regions of no TTC uptake. Binary masks were then created to distinguish ablated tissue (defined as no TTC uptake) from non–ablated tissue (reduced or full TTC uptake) and to distinguish treated tissue (reduced or no TTC uptake) from untreated tissue (full TTC uptake). Separate masks were created for liver and tumor regions for direct comparison to echo decorrelation and IBS images.

2.2.6 Statistical analysis

Separate statistical analyses were performed for focused exposures in liver and VX2 tumor, unfocused exposures in liver and VX2 tumor, and the combination of all exposures in liver and VX2 tumor.

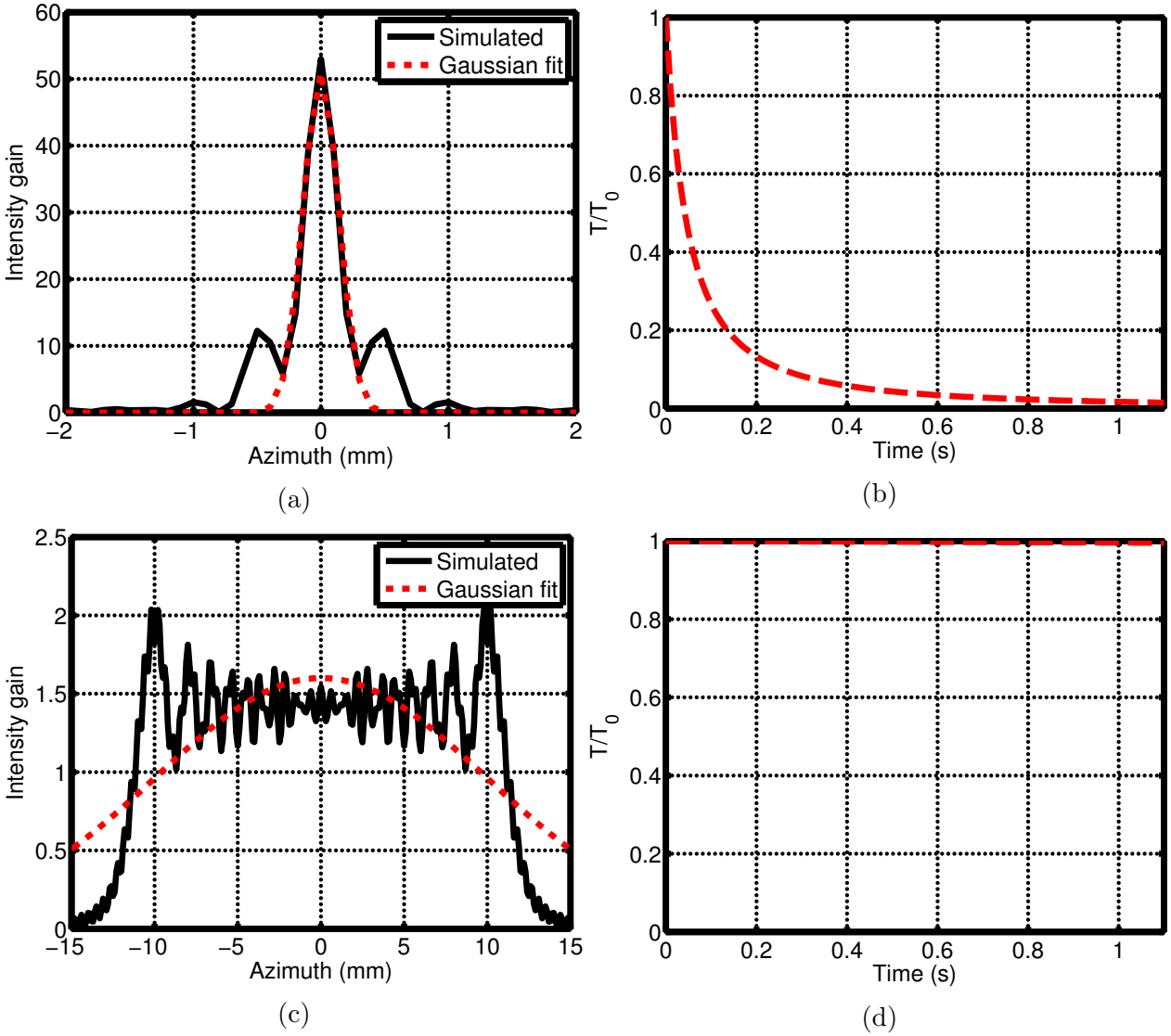

Figure 2.4: Gaussian fits for the simulated focused (Figure 2.4a) and unfocused (Figure 2.4c) intensity beam shapes used to approximate σ in Equation 2.3. The T/T_0 decay for HIFU (Figure 2.4b) and bulk (Figure 2.4d) ablation illustrates that effects of the delay times were not negligible for the HIFU ablations imaged 1.1 s after the end of sonication, but that these effects were negligible for unfocused ablations imaged 1.1 s after sonication.

Focused exposure trials were excluded from the final analysis if the post–focal lesion extended beyond a depth 2 mm from the dorsal side of the liver lobe. Additionally, focused exposures imaged > 1 s after sonication were excluded. Focused and unfocused trials were also excluded if the corresponding TTC–stained gross histology was inconclusive. Twenty–six trials were excluded, leaving 23 for further analysis.

Significant reduction of noise decorrelation by correction was tested by comparing $\log_{10}$–scaled mean echo decorrelation in non–ablated regions before and after correction using a paired one–tailed t test with significance criterion $p < 0.05$.

Significant increase of $\log_{10}$–scaled mean echo decorrelation within ablated regions was tested by comparing $\log_{10}$–scaled mean echo decorrelation in the ablated regions and non–ablated regions using unpaired and paired one–tailed t tests with the significance criterion $p < 0.05$. Significant differences between $\log_{10}$–scaled mean echo decorrelation in non–ablated liver and non–ablated VX2 tumor were tested using unpaired and paired two–tailed t tests with the significance criterion $p < 0.05$. Significant differences between $\log_{10}$–scaled mean echo decorrelation in ablated liver and ablated VX2 tumor were tested using unpaired and paired two–tailed t tests with the significance criterion $p < 0.05$. The unpaired t test was used to detect differences in the collective average $\log_{10}$–scaled mean echo decorrelation. The paired t test was used to detect differences between paired (i.e., non-ablated and ablated regions in each tissue section) $\log_{10}$–scaled mean echo decorrelation. The same analysis described above was also performed for decibel–scaled mean IBS.

Receiver operating characteristic (ROC) curves were constructed by comparing thresholded corrected echo decorrelation and IBS images to tissue ablation maps. The ROC curve is the false–positive rate ($1-$specificity) versus the true–positive rate (sensitivity) for each threshold value (Hanley et al., 1982). The $1-$specificity and the sensitivity are defined as

$$\text{Sensitivity} = \frac{\text{TP}}{\text{TP} + \text{FN}} \tag{2.5}$$

$$1 - \text{specificity} = \frac{\text{FP}}{\text{FP} + \text{TN}}, \tag{2.6}$$

where TP is the number of correct positive classifications, TN is the number of correct negative classifications, FP is the number of incorrect positive classifications, and FN is the number of incorrect negative classifications.

The area under the curve (AUC) was used to determine the predictive success of parameter images. An AUC of 1 indicates that the parameter image predicted the tissue ablation perfectly, whereas an AUC of 0.5 means that the prediction was no better than chance (Hanley et al., 1982).

Thresholds for optimal prediction of tissue ablation for echo decorrelation and IBS were determined by selecting the threshold corresponding to the point nearest to the top left–hand corner of the ROC plot (Krzanowski et al., 2009). This approaches weights the importance of specificity and sensitivity for ablation prediction equally.

For assessment of statistical significance, effective sample sizes (N_{eff}) were determined by estimating the number of independent ablation predictions from the total number of samples (N_{total}):

$$\frac{N_{\text{eff}}}{N_{\text{total}}} = \frac{\Delta z \Delta y \gamma}{d^2}, \tag{2.7}$$

where $\gamma = \pi/\sqrt{12}$ is the number of unit–diameter circles per unit–area rectangle for the maximum hexagonal packing density (Subramanian et al., 2014). The range and azimuthal echo decorrelation map pixel dimensions are Δz and Δy. In Equation 2.7, d is the Gaussian

full width at half maximum:

$$d = 2\sqrt{2\ln(2)}\sigma, \tag{2.8}$$

where σ=1.0 mm is the Gaussian width parameter (Subramanian et al., 2014). The statistical significance of measured AUC values vs. the null hypothesis (AUC=0.5) was then calculated in MATLAB using a general model for the AUC standard error (Hanley et al., 1982) (significance criterion p <0.05, one–tailed). Statistical significance of differences between AUC values for corrected echo decorrelation and IBS was calculated in R (pROC package; R Foundation for statistical Computing, Vienna, Austria) by calculating the Z–statistic (Z_{total}) for N_{total} using the method of DeLong et al. (1988) (significance criterion p <0.05, two–tailed). The effective p–value was determined by correcting Z_{total} using the equation:

$$Z_{\text{eff}} = \frac{Z_{\text{total}}}{\sqrt{\frac{N_{\text{total}}}{N_{\text{eff}}}}}, \tag{2.9}$$

where Z_{eff} is the effective Z–statistic. The effective significance $p_{\text{effective}}$ (significance criterion p <0.05, two–tailed) was then determined from Z_{eff} using the cumulative distribution function (cdf) and the equation

$$p_{\text{effective}} = 2(1 - \text{cdf}(Z_{\text{eff}})). \tag{2.10}$$

2.2.7 Analysis of inter–frame time effects

To determine the effect of imaging inter–frame time in echo decorrelation and IBS ablation prediction performance, uncorrected and corrected echo decorrelation and IBS images were constructed for τ (inter–frame time) = 8.5, 42.4, 84.7, 127.1, 169.5, 211.9, 254.2, 508.5, and 847.5 ms for focused and unfocused exposures in liver and VX2 tumor. Echo decorre-

lation and IBS images were registered and quantitatively compared with the corresponding histology and the ROC curves and AUCs were computed as described in the previous section.

2.3 Results

Sham cumulative decorrelation (I), tissue histology (II), cumulative decorrelation (III), and integrated backscatter (IBS) (IV) images for all of the 23 trials are shown in Figure 2.5 A–W. In the echo decorrelation and IBS images, the threshold for optimal prediction of ablation ($\log_{10}$–scaled echo decorrelation per millisecond: -3.1; IBS: 3.86 dB) is indicated by the yellow line. The white line indicates the tissue boundaries as seen in the B–mode images. In the TTC–stained tissue sections, the red, blue, green, and black lines indicate tissue, treated, ablated, and tumor regions. For focused exposures, Figures 2.5 A–M, generally better correspondence with histology was seen for corrected echo decorrelation than for IBS. For unfocused exposures, Figures 2.5 N–W, comparable correspondence between IBS (IV), corrected echo decorrelation (III), and histology (II) was seen.

Elevated echo decorrelation within non–ablated liver regions due to noise and motion was significantly reduced using Equation 1.7 for the focused exposures, unfocused exposures, and all exposures combined (Table 2.1). Decorrelation was significantly reduced in non–ablated tumor regions for focused exposures and all exposures combined; however, there was not a significant reduction for the unfocused exposures. Reduction of decorrelation within ablated tissue and tumor regions was marginally significant for focused exposures and unfocused exposures and significant for the all exposures combined.

The mean and standard error values of the $\log_{10}$–scaled mean corrected echo decorrelation per millisecond and the decibel–scaled mean IBS within non–ablated and ablated regions for unfocused exposures in liver (N=10) and tumor (N=8), focused exposures in liver (N=13) and tumor (N=6) and the combined exposures in liver (N=23) and tumor (N=14) are

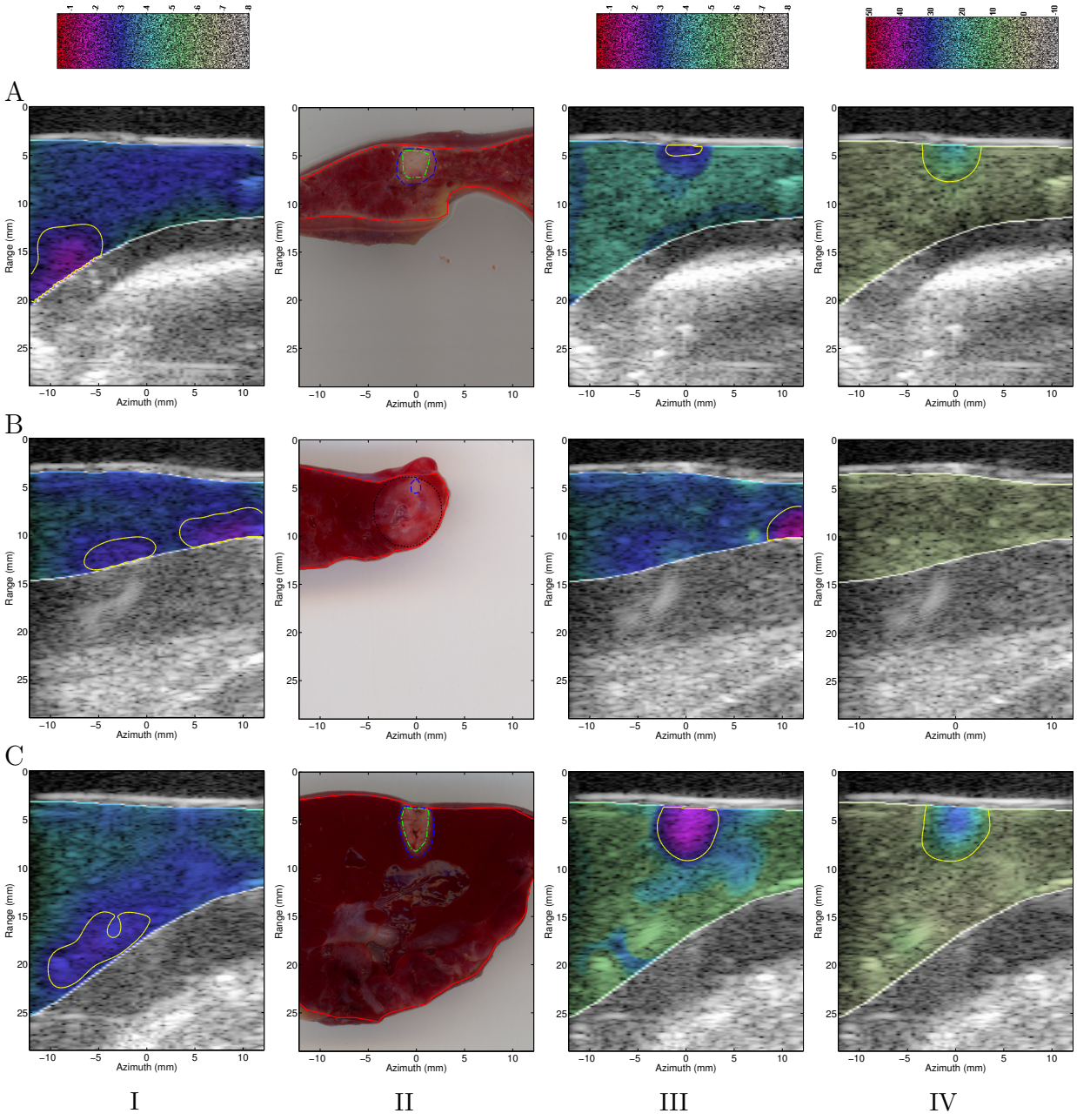

Figure 2.5: From left to right are the $\log_{10}$-scaled sham cumulative echo decorrelation (I), corresponding segmented triphenyl terazolium chloride (TTC) stained image–ablated plane histology (II), $\log_{10}$-scaled cumulative corrected echo decorrelation (III), and decibel–scaled cumulative integrated backscatter (IBS) (IV) for HIFU ablation (sub–figures A–M) and bulk ablation (sub–figures N–W). The white line indicates tissue boundaries as seen in the B–mode images. In the echo decorrelation and IBS images, the threshold for optimal prediction of ablation ($\log_{10}$–scaled echo decorrelation per millisecond: -3.1; IBS: 3.86 dB) is indicated by the yellow–dotted line. In the TTC–stained tissue sections, the red, blue, green, and black boundaries indicate the tissue, treated, ablated, and tumor regions.

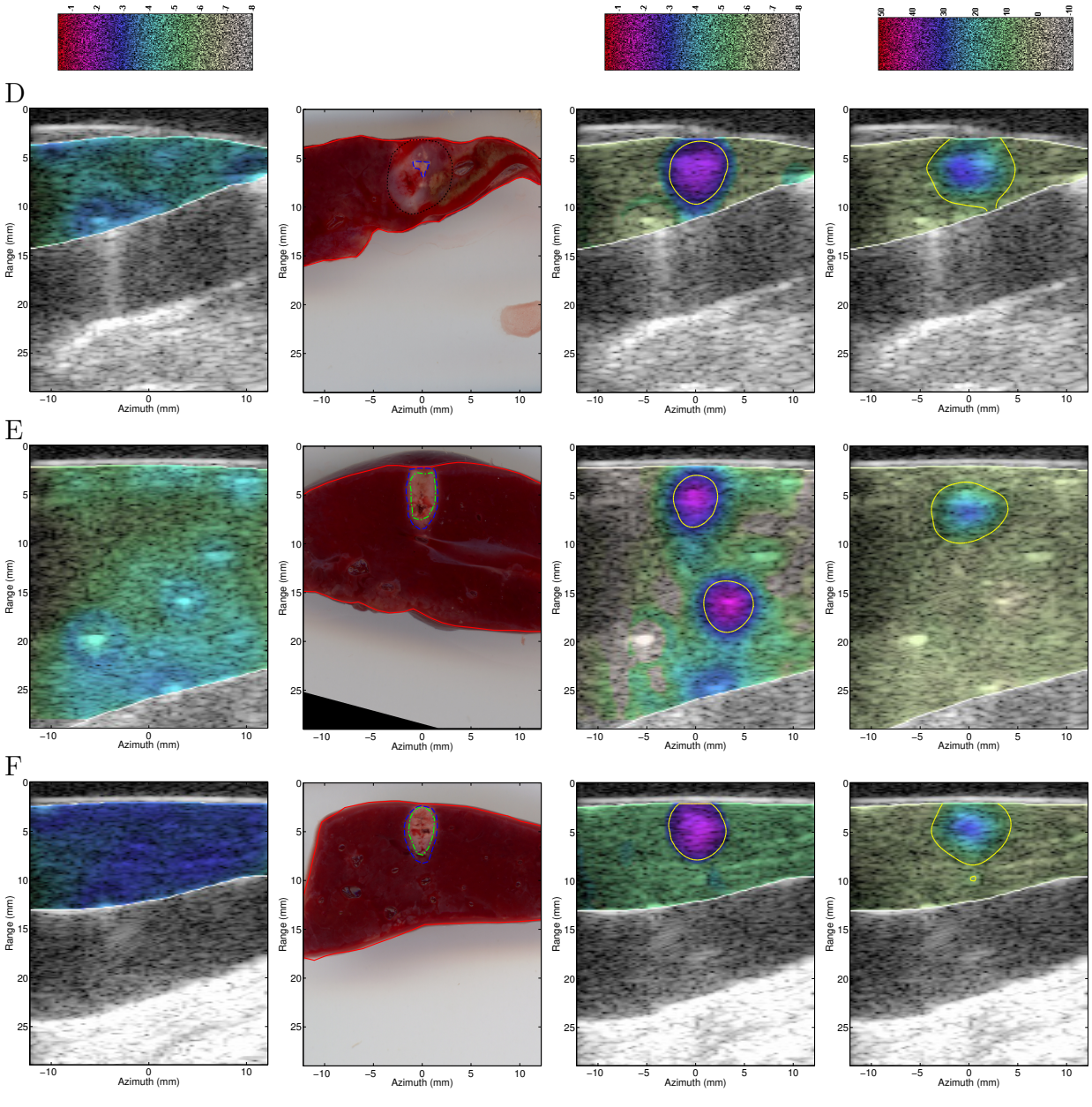

Figure 2.5 continued.

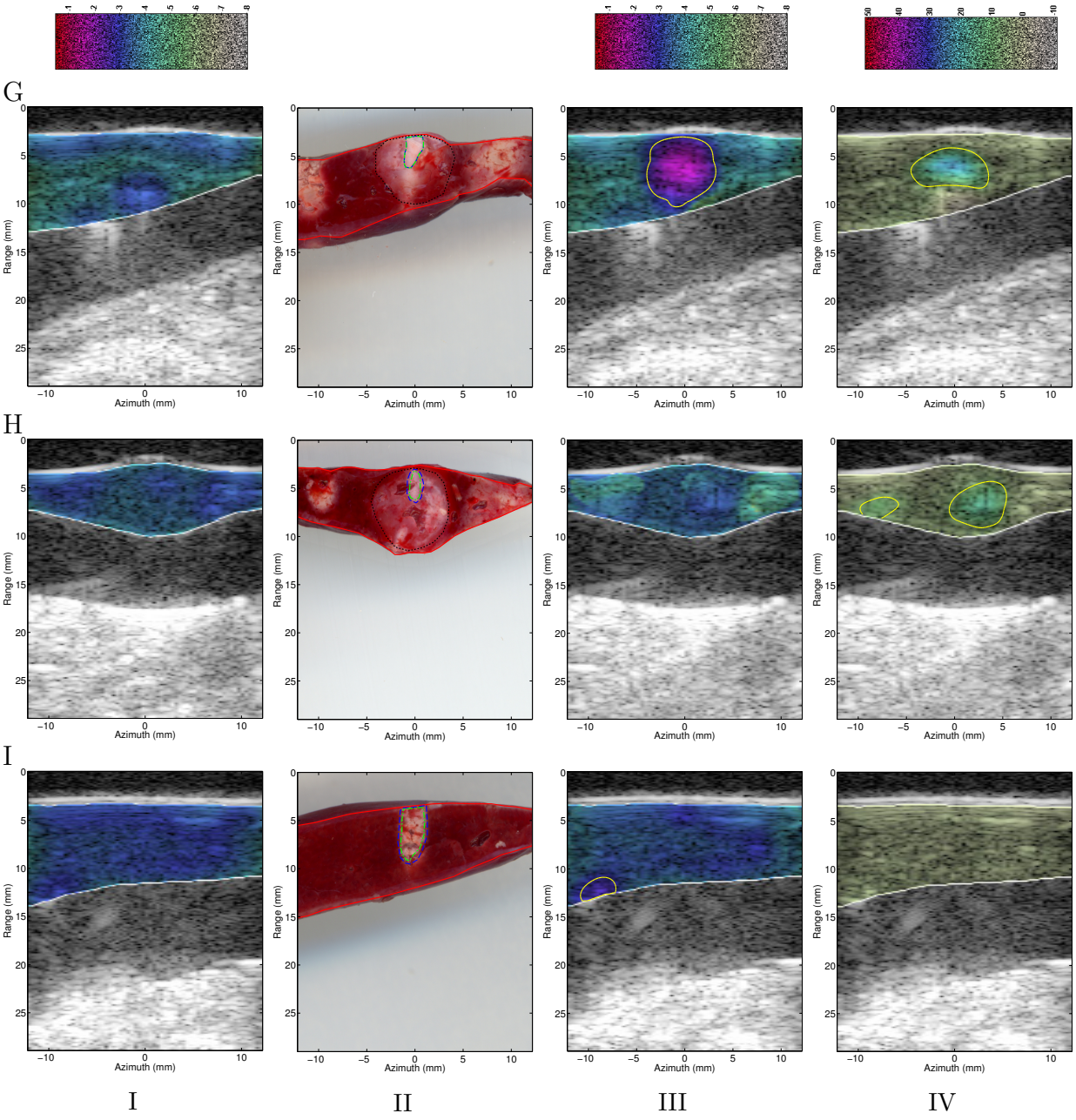

Figure 2.5 continued.

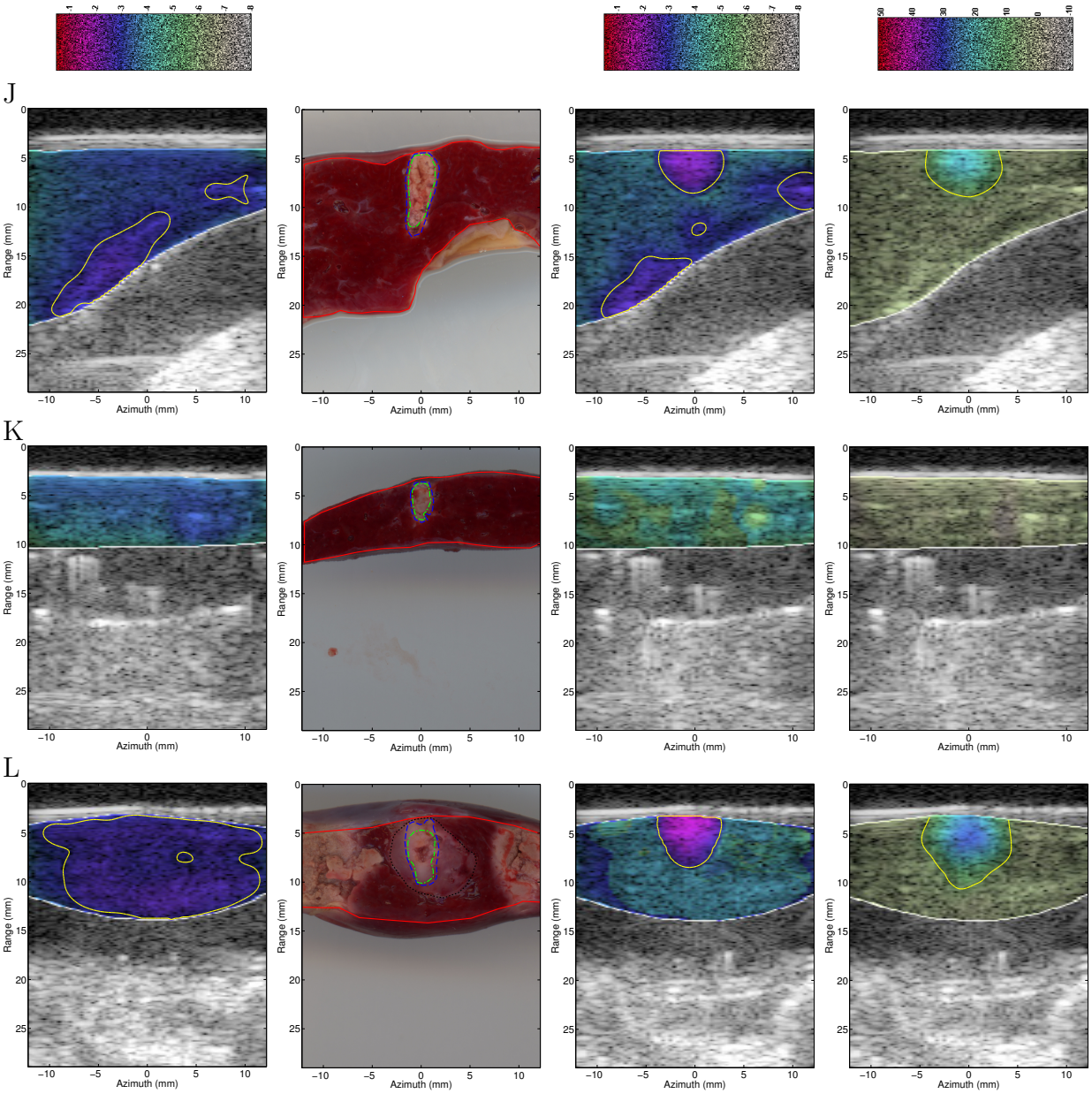

Figure 2.5 continued.

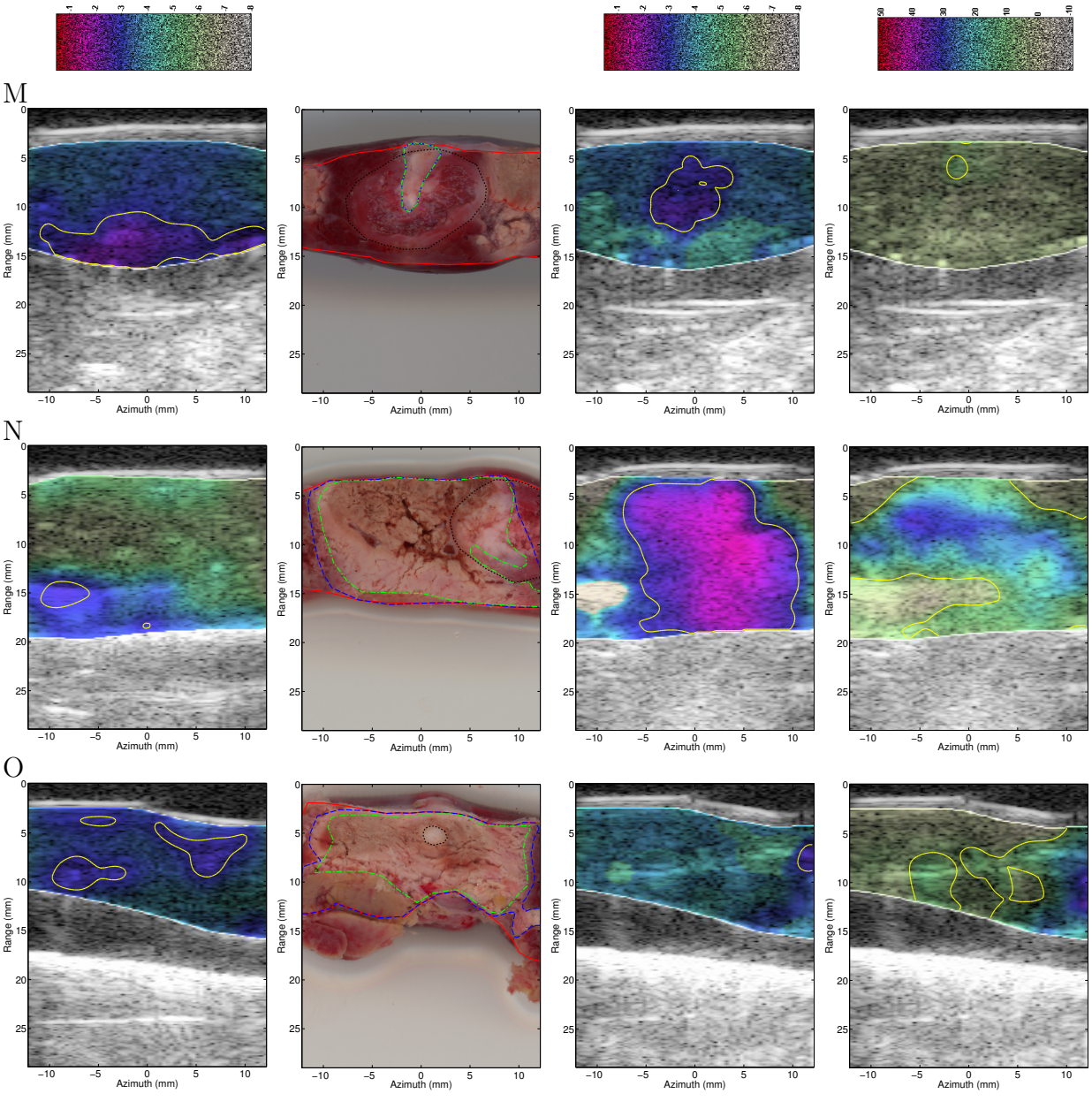

Figure 2.5 continued.

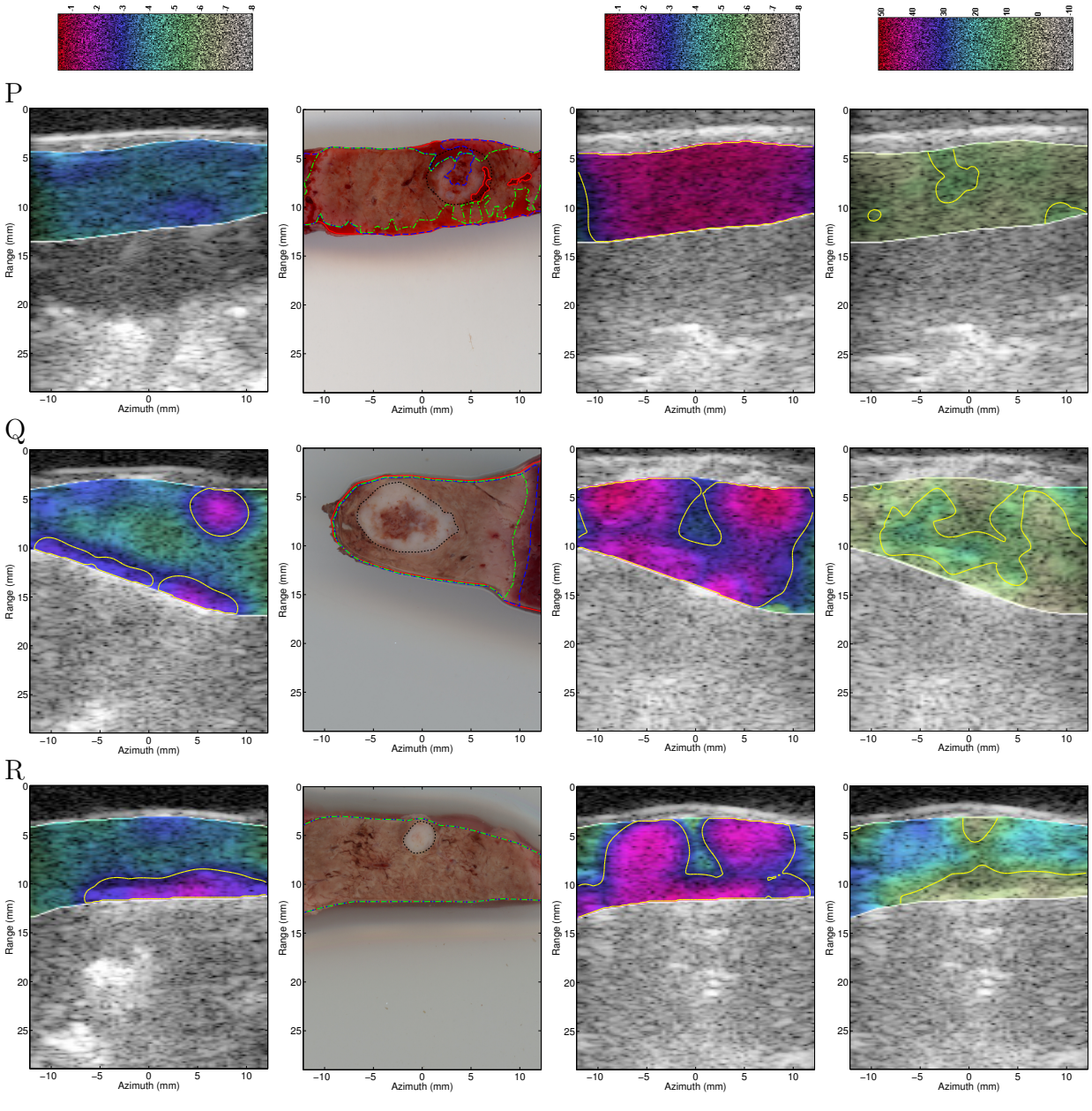

Figure 2.5 continued.

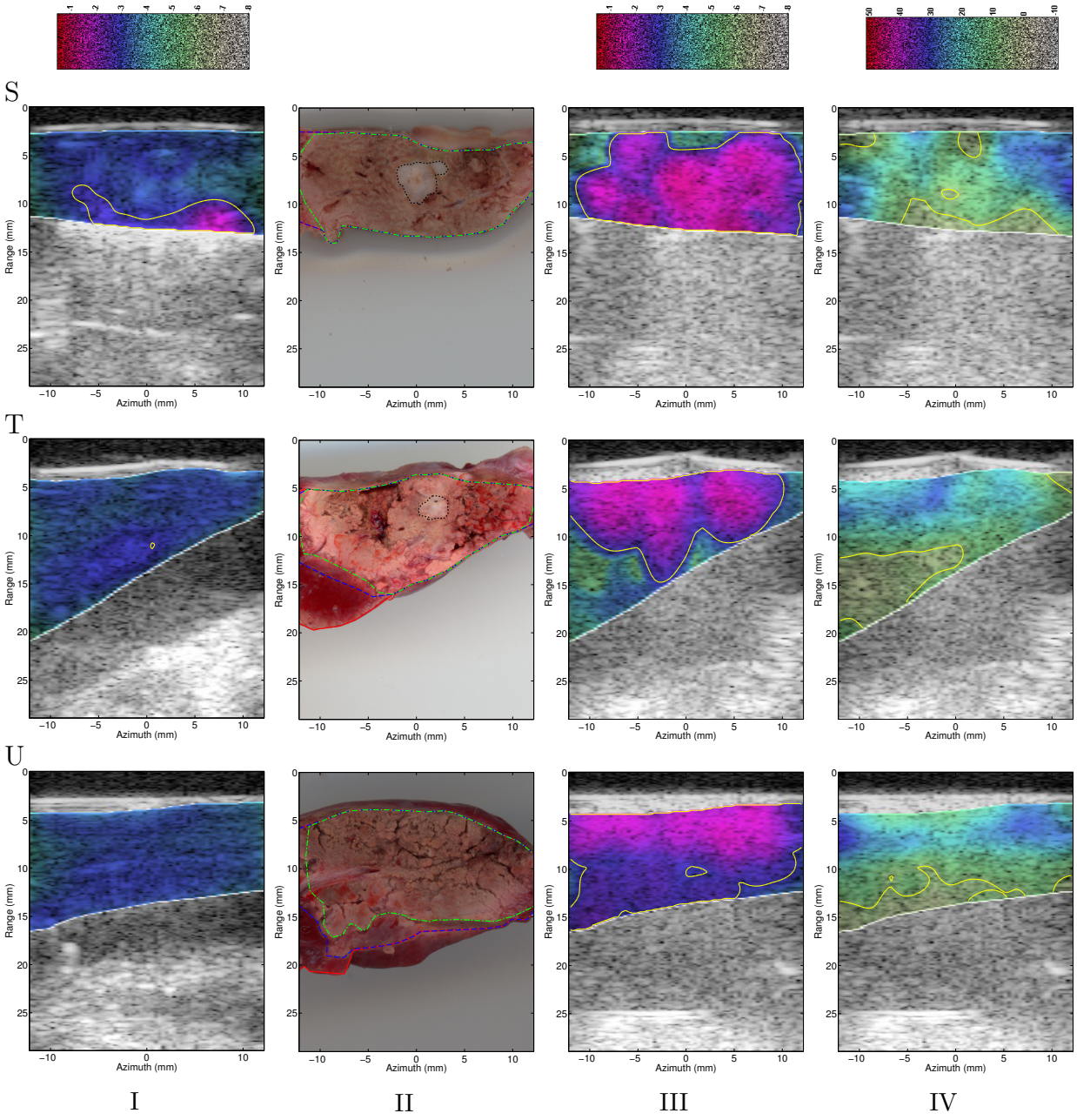

Figure 2.5 continued.

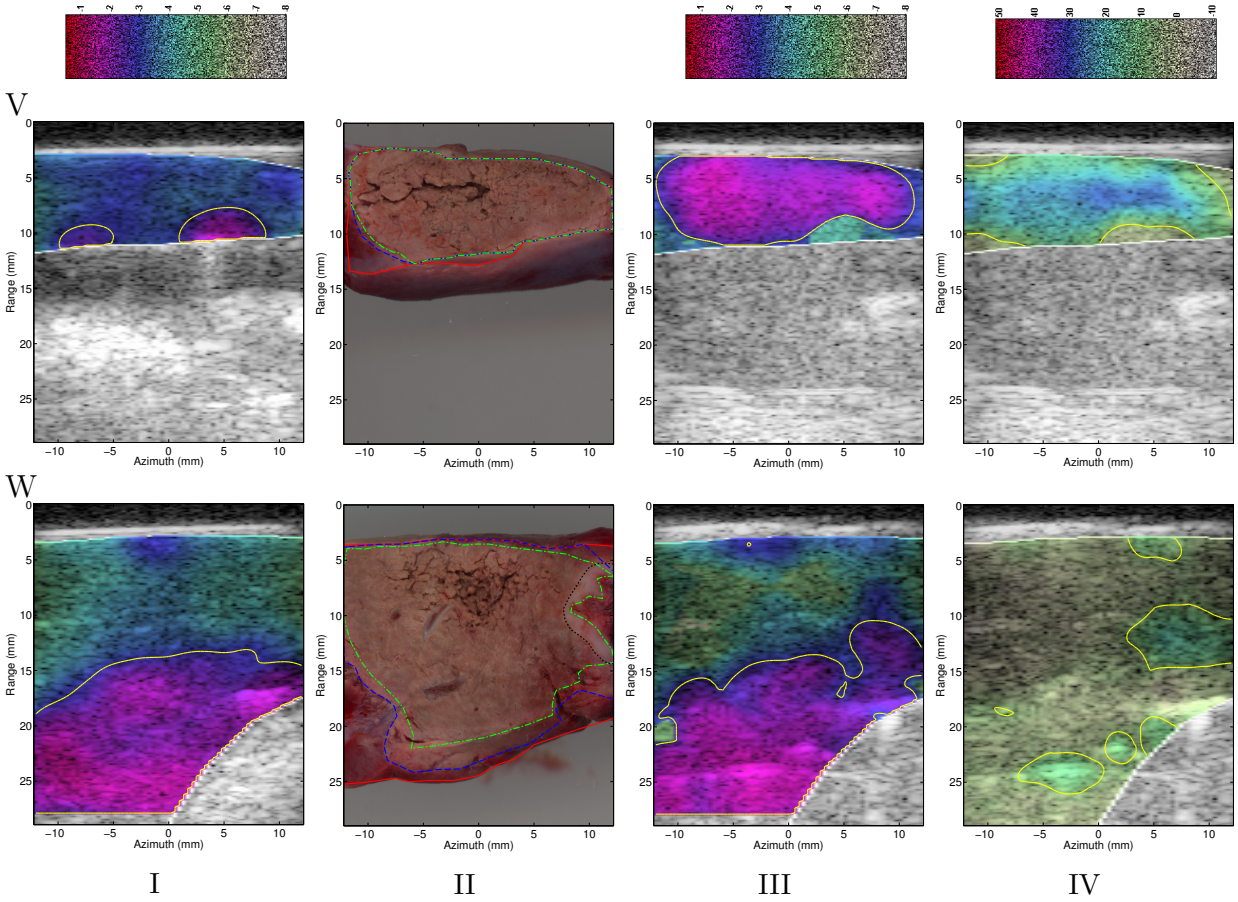

Figure 2.5 continued.

Exposure	Liver	VX2 tumor
HIFU	-6.03 $(2.97{\cdot}10^{-5})$	-2.73 (0.02)
Bulk	-2.78 (0.01)	-1.07 (0.20)
All exposures combined	-5.67 $(6.35{\cdot}10^{-6})$	-2.40 (0.02)

Table 2.1: The t–statistic and p–value for comparisons between $\log_{10}$–scaled mean echo decorrelation in non–ablated liver and VX2 tumor regions before and after correction.

Exposure	Liver	VX2 tumor
HIFU	-2.07 (0.04)	-2.35 (0.05)
Bulk	-1.92 (0.04)	-2.20 (0.03)
All Exposures Combined	-2.71 $(7.46{\cdot}10^{-3})$	-2.33 (0.02)

Table 2.2: The t–statistic and p–value for comparisons between $\log_{10}$–scaled mean echo decorrelation in ablated liver and VX2 tumor regions before and after correction.

illustrated in Figures 2.13, 2.14, and 2.15 and tabulated in Table 2.3.

For unpaired comparisons, the $\log_{10}$–scaled mean corrected echo decorrelation within ablated liver regions was significantly greater than in non–ablated regions for focused exposures, unfocused exposures, and all exposures combined (Tables 2.4). In VX2 tumor, the $\log_{10}$–scaled mean corrected echo decorrelation within ablated regions was marginally greater than in non–ablated regions for focused exposures, unfocused exposures, and all exposures combined. Differences in the $\log_{10}$–scaled mean corrected echo decorrelation within non—ablated liver and tumor were significant for focused exposures, not significant for unfocused exposures and marginally significant for all exposures combined. The $\log_{10}$–scaled mean corrected echo decorrelation within ablated liver and tumor were not significantly different.

For unpaired comparisons, the decibel–scaled mean IBS within ablated liver regions was significantly greater than in non–ablated regions for focused exposures and all exposures combined and not significant greater for unfocused exposures (Table 2.6). In VX2 tumor, the decibel–scaled mean IBS within ablated regions was marginally greater than in non–ablated regions for focused exposures, unfocused exposures, and all exposures combined. Differences in the decibel–scaled mean IBS within non–ablated liver and tumor were significant for focused exposures but not significant for unfocused exposures and all exposures combined. The decibel–scaled mean IBS within ablated liver and tumor were not significantly different.

	Liver		VX2 tumor	
Exposure	Non–ablated	Ablated	Non–ablated	Ablated
HIFU	−3.88 (0.14)	−3.04 (0.30)	−3.06 (0.23)	−2.89 (0.40)
Bulk	−3.05 (0.30)	−2.32 (0.23)	−2.57 (0.70)	−2.47 (0.31)
All exposures combined	−3.54 (0.17)	−2.64 (0.20)	−2.90 (0.26)	−2.61 (0.24)

Table 2.3: Mean and standard error of $\log_{10}$–scaled mean echo decorrelation per millisecond in non–ablated and ablated regions.

The results for paired comparisons are tabulated in Tables 2.7 and 2.8. In liver, the $\log_{10}$–

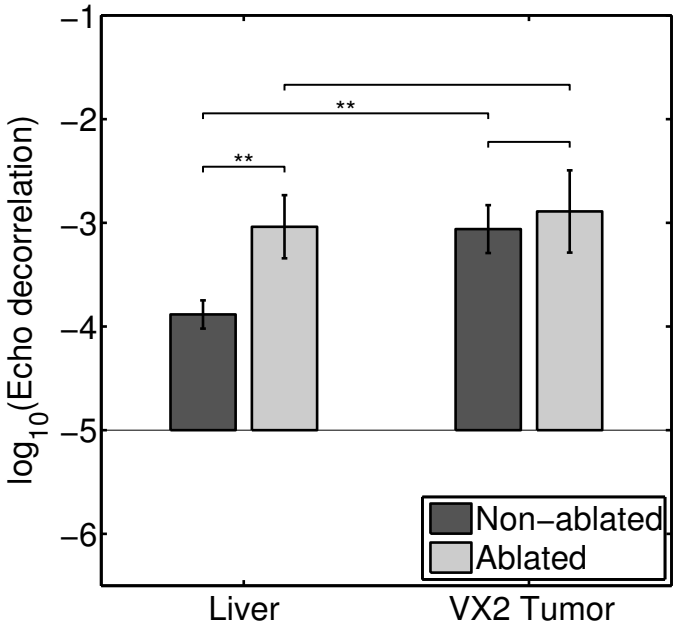

(a)

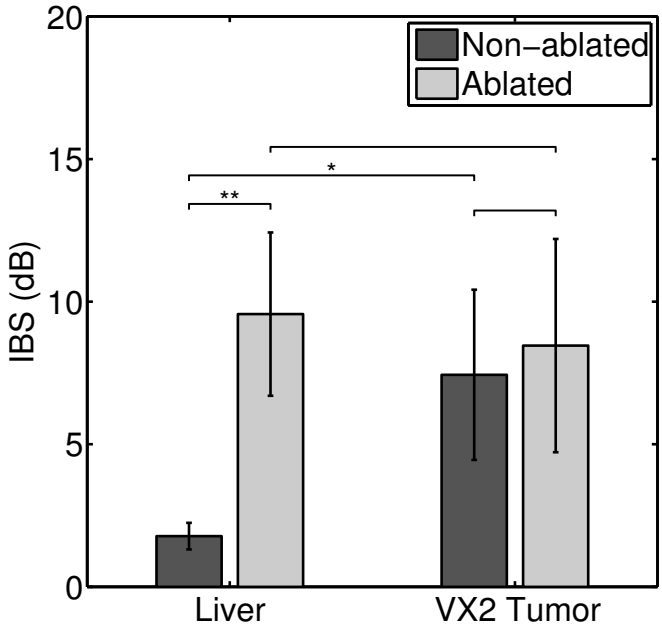

(b)

Figure 2.13: Mean and standard error of corrected $\log_{10}$–scaled echo decorrelation per millisecond (Figure 2.13a) and decibel–scaled IBS (Figure 2.13b) in non–ablated and ablated regions for focused exposures in liver and VX2 tumor. The single, double, and triple asterisks correspond to $p \leq 0.05$, $p \leq 10^{-2}$, and $p \leq 10^{-3}$.

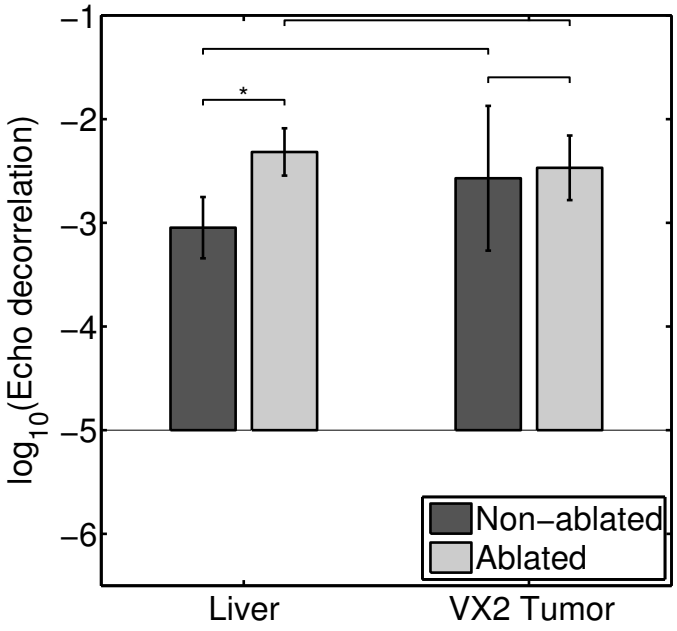

(a)

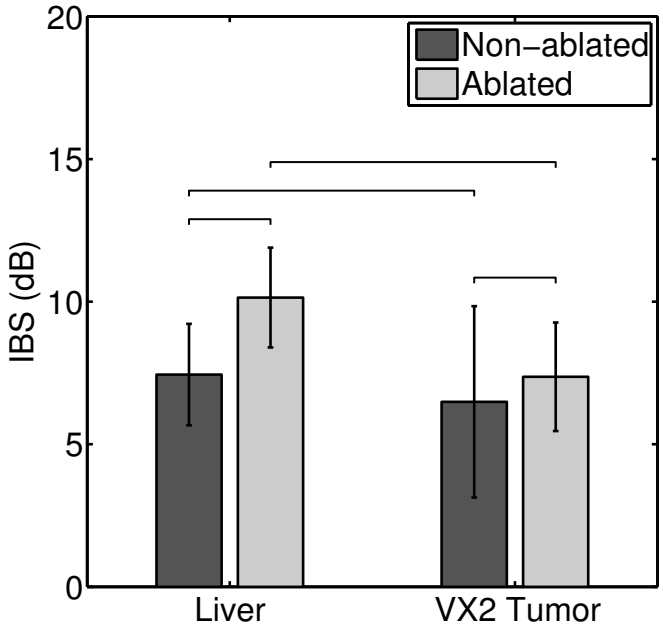

(b)

Figure 2.14: Mean and standard error of corrected $\log_{10}$–scaled echo decorrelation per millisecond (Figure 2.14a) and decibel–scaled IBS (Figure 2.14b) in non–ablated and ablated regions for unfocused exposures in liver and VX2 tumor. The single, double, and triple asterisks correspond to $p \leq 0.05$, $p \leq 10^{-2}$, and $p \leq 10^{-3}$.

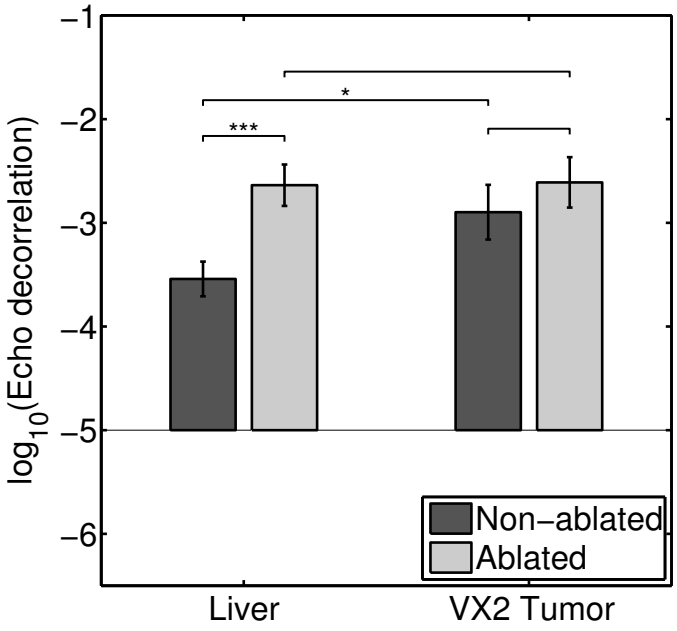

(a)

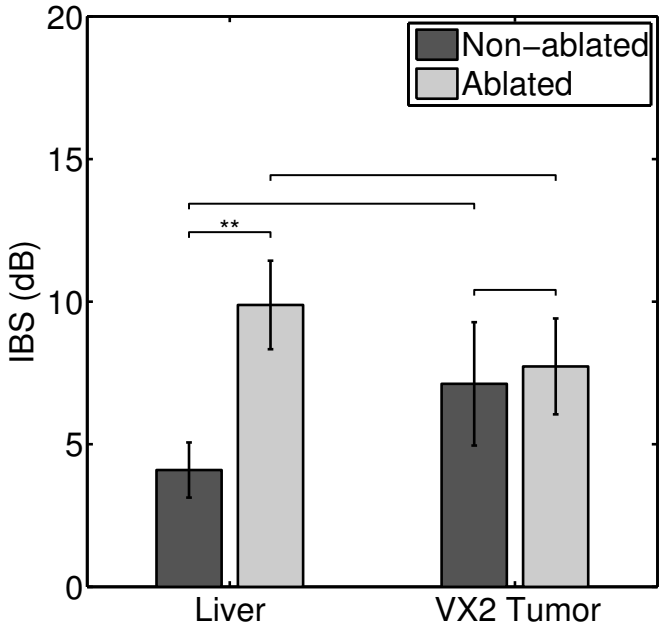

(b)

Figure 2.15: Mean and standard error of corrected $\log_{10}$–scaled echo decorrelation per millisecond (Figure 2.15a) and decibel–scaled IBS (Figure 2.15b) in non–ablated and ablated regions for the group of all exposures in liver and VX2 tumor. The single, double, and triple asterisks correspond to $p \leq 0.05$, $p \leq 10^{-2}$, and $p \leq 10^{-3}$.

	Non–ablated vs. ablated		Liver vs. VX2 tumor	
Exposure	Liver	VX2 tumor	Non–ablated	Ablated
HIFU	2.89 ($4.71 \cdot 10^{-3}$)	0.40 (0.35)	3.25 ($4.73 \cdot 10^{-3}$)	0.29 (0.78)
Bulk	1.98 (0.03)	0.15 (0.44)	0.74 (0.47)	−0.41 (0.69)
All exposures combined	3.50 ($6.02 \cdot 10^{-4}$)	0.80 (0.22)	2.07 (0.05)	0.09 (0.93)

Table 2.4: The unpaired t–statistic and p–value for comparisons between $\log_{10}$–scaled mean echo decorrelation in ablated and non–ablated liver and VX2 tumor regions.

	Liver		VX2 tumor	
Exposure	Non–ablated	Ablated	Non–ablated	Ablated
HIFU	1.78 (0.47)	9.56 (2.86)	7.43 (2.98)	8.46 (3.74)
Bulk	7.44 (1.78)	10.14 (1.75)	6.49 (3.37)	7.36 (1.90)
All exposures combined	4.10 (0.97)	9.89 (1.55)	7.12 (2.16)	7.73 (1.68)

Table 2.5: Mean and standard error of decibel–scaled mean integrated backscatter in non–ablated and ablated regions.

	Non–ablated vs. ablated		Liver vs. VX2 tumor	
Exposure	Liver	VX2 tumor	Non–ablated	Ablated
HIFU	3.40 ($1.50 \cdot 10^{-3}$)	0.22 (0.42)	2.72 (0.01)	−0.23 (0.82)
Bulk	1.08 (0.15)	0.24 (0.41)	−0.26 (0.80)	−1.07 (0.30)
All exposures combined	3.28 ($1.10 \cdot 10^{-3}$)	0.23 (0.41)	1.48 (0.15)	−0.92 (0.37)

Table 2.6: The unpaired t–statistic and p–value for comparisons between decibel–scaled mean integrated backscatter in ablated and non–ablated liver and VX2 tumor.

scaled mean corrected echo decorrelation within ablated regions was significantly greater than in non–ablated regions for focused exposures, unfocused exposures and all exposures combined. In VX2 tumor, the $\log_{10}$–scaled mean corrected echo decorrelation within ablated regions was marginally greater than in non–ablated regions for focused exposures and unfocused exposures and marginally significant for all exposures combined. Differences in the $\log_{10}$–scaled mean corrected echo decorrelation within non—ablated liver and tumor were significant for focused exposures and not significant for unfocused exposures and for all exposures combined. The $\log_{10}$–scaled mean corrected echo decorrelation within ablated liver and tumor were not significantly different.

In liver, the decibel–scaled mean IBS within ablated regions were significantly greater than in non–ablated regions for focused exposures and all exposures combined and marginally greater for unfocused exposures (Table 2.8). In VX2 tumor, the decibel–scaled mean IBS within ablated regions was not significantly greater than in non–ablated regions for focused exposures and unfocused exposures and was significantly greater for all exposures combined. Differences in the decibel–scaled mean IBS within non—ablated liver and tumor were not significant for focused exposures and unfocused exposures but were marginally significant for all exposures combined. The decibel–scaled mean IBS within ablated liver and tumor were not significantly different.

	Non-ablated vs. ablated		Liver vs. VX2 tumor	
Exposure	Liver	VX2 Tumor	Non-ablated	Ablated
HIFU	4.42 ($1.54 \cdot 10^{-3}$)	1.44 (0.12)	2.91 (0.03)	NA
Bulk	2.23 (0.03)	1.69 (0.12)	−0.59 (0.62)	−0.91(0.39)
All exposures combined	4.07 ($4.49 \cdot 10^{-4}$)	2.18 (0.04)	1.48 (0.18)	−0.54 (0.60)

Table 2.7: The paired t test t–statistic and p–value for comparisons between $\log_{10}$–scaled mean echo decorrelation in ablated and non–ablated liver and VX2 tumor regions.

Corresponding ROC curves for each group of exposures are shown in Figures 2.16, 2.17,

	Non-ablated vs. ablated		Liver vs. VX2 tumor	
Exposure	Liver	VX2 Tumor	Non-ablated	Ablated
HIFU	3.46 ($5.27 \cdot 10^{-3}$)	1.29 (0.14)	2.31 (0.07)	NA
Bulk	1.31 (0.11)	2.01 (0.09)	3.60 (0.07)	−1.25 (0.25)
All exposures combined	3.20 ($2.78 \cdot 10^{-3}$)	2.22 (0.03)	2.36 (0.05)	−1.26 (0.24)

Table 2.8: The paired t–statistic and p–value for comparisons between decibel–scaled mean integrated backscatter in ablated and non–ablated liver and VX2 tumor.

and 2.18. The summary statistics for the ROC curve comparisons are tabulated in Tables 2.9– 2.13. Treated and ablated regions in liver were predicted significantly better than chance (AUC=0.5) by corrected echo decorrelation and IBS for focused exposures, unfocused exposures and all exposures combined (Tables 2.9 and 2.10). Treated and ablated regions in VX2 tumor were predicted significantly better than chance by corrected echo decorrelation for unfocused exposures and all exposures combined (Table 2.11). Treated and ablated regions in VX2 tumor were not predicted significantly better than chance by corrected echo decorrelation for focused exposures. Treated regions in VX2 tumor were predicted significantly better than chance by IBS for focused exposures, unfocused exposures and all exposures combined (Table 2.12). IBS only predicted ablated VX2 tumor significantly better than chance for all exposures combined.

	Liver	
Exposure	Treated	Ablated
HIFU	8.22 ($< 1.00 \cdot 10^{-12}$)	6.74 ($< 1.00 \cdot 10^{-12}$)
Bulk	2.95 ($1.60 \cdot 10^{-3}$)	3.30 ($5.00 \cdot 10^{-3}$)
All exposures combined	24.17 ($< 1.00 \cdot 10^{-12}$)	20.97 ($< 1.00 \cdot 10^{-12}$)

Table 2.9: The z–statistic and p–value for comparisons between AUC=0.5 and echo decorrelation ablation prediction of treated and ablated liver regions.

Table 2.13 summarizes the comparisons between echo decorrelation and IBS ablation prediction performance. In liver, corrected echo decorrelation predicted significantly better

	Liver	
Exposure	Treated	Ablated
HIFU	3.80 ($7.16 \cdot 10^{-5}$)	3.01 ($1.30 \cdot 10^{-4}$)
Bulk	3.11 ($9.00 \cdot 10^{-4}$)	4.36 ($1.00 \cdot 10^{-12}$)
All exposures combined	17.35 ($< 1.00 \cdot 10^{-12}$)	15.83 ($< 1.00 \cdot 10^{-12}$)

Table 2.10: The z–statistic and p–value for comparisons between AUC=0.5 and IBS ablation prediction of treated and ablated liver regions.

	VX2 tumor	
Exposure	Treated	Ablated
HIFU	1.44 (0.08)	1.31 (0.09)
Bulk	1.77 (0.04)	1.80 (0.04)
All exposures combined	3.54 ($2.00 \cdot 10^{-4}$)	3.80 ($1.00 \cdot 10^{-4}$)

Table 2.11: The z–statistic and p–value for comparisons between AUC=0.5 and echo decorrelation ablation prediction of treated and ablated VX2 tumor regions.

	VX2 tumor	
Exposure	Treated	Ablated
HIFU	1.73 (0.04)	1.19 (0.12)
Bulk	1.72 (0.04)	0.33 (0.37)
All exposures combined	3.36 ($4.00 \cdot 10^{-4}$)	2.33 (0.01)

Table 2.12: The z–statistic and p–value for comparisons between AUC=0.5 and IBS ablation prediction of treated and ablated VX2 regions.

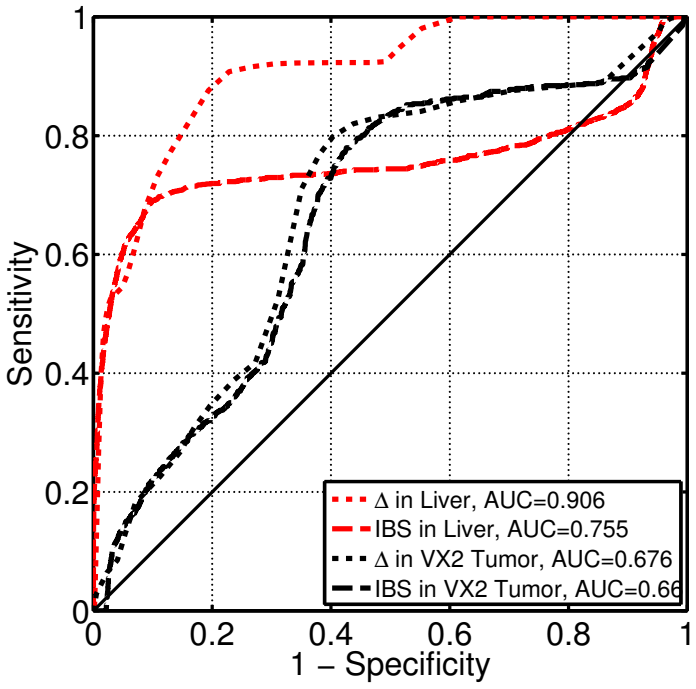

(a)

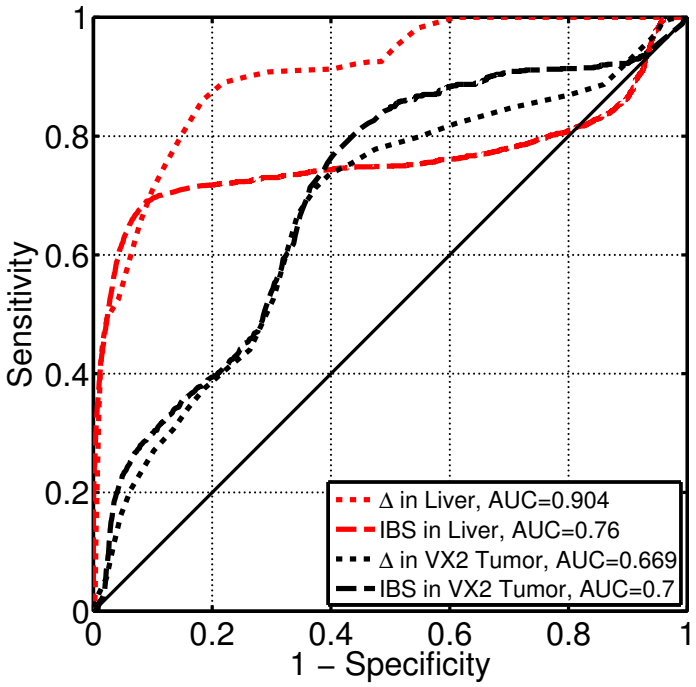

(b)

Figure 2.16: ROC curves illustrating prediction performance for tissue ablation (no TTC uptake) (Figure 2.16a) and tissue treatment (reduced or no TTC uptake) (Figure 2.16b) by corrected echo decorrelation (dotted lines) and IBS (dash–dotted lines) for focused exposures in liver (red lines) and VX2 tumor (black lines).

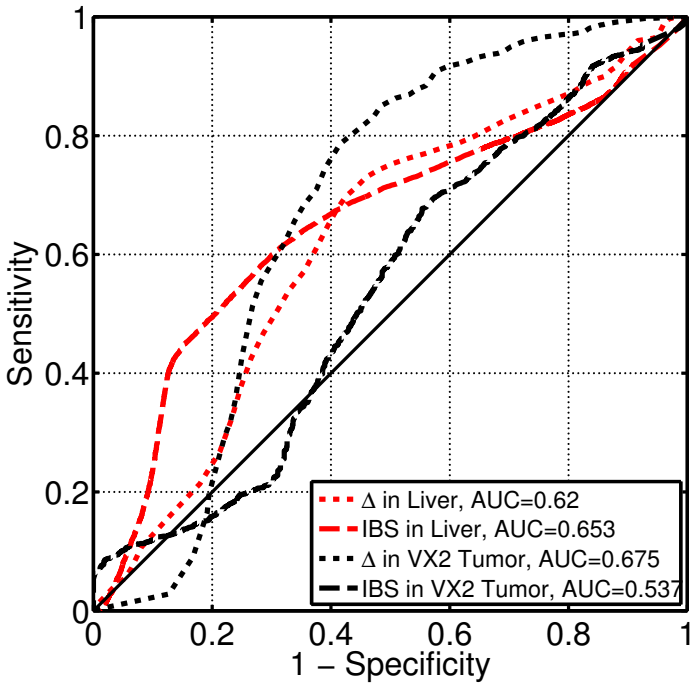

(a)

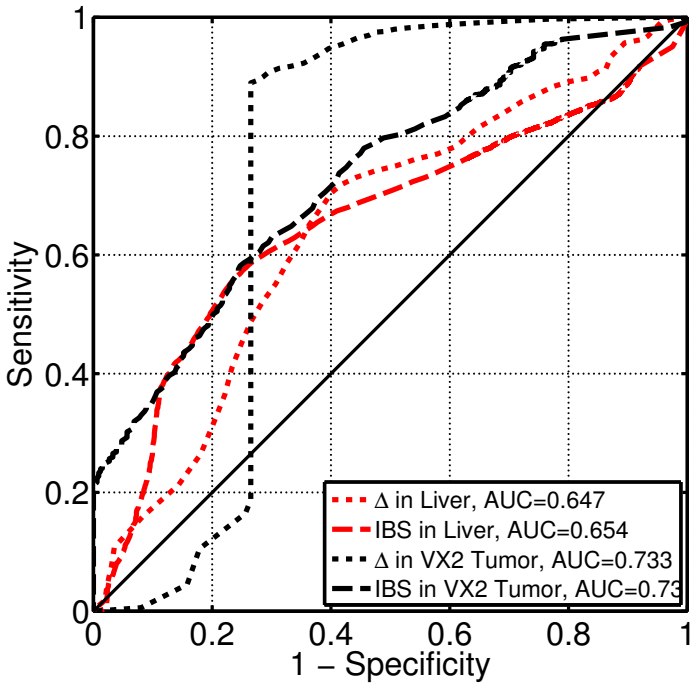

(b)

Figure 2.17: ROC curves illustrating prediction performance for tissue ablation (no TTC uptake) (Figure 2.17a) and tissue treatment (reduced or no TTC uptake) (Figure 2.17b) by corrected echo decorrelation (dotted lines) and IBS (dash–dotted lines) for unfocused exposures in liver (red lines) and VX2 tumor (black lines).

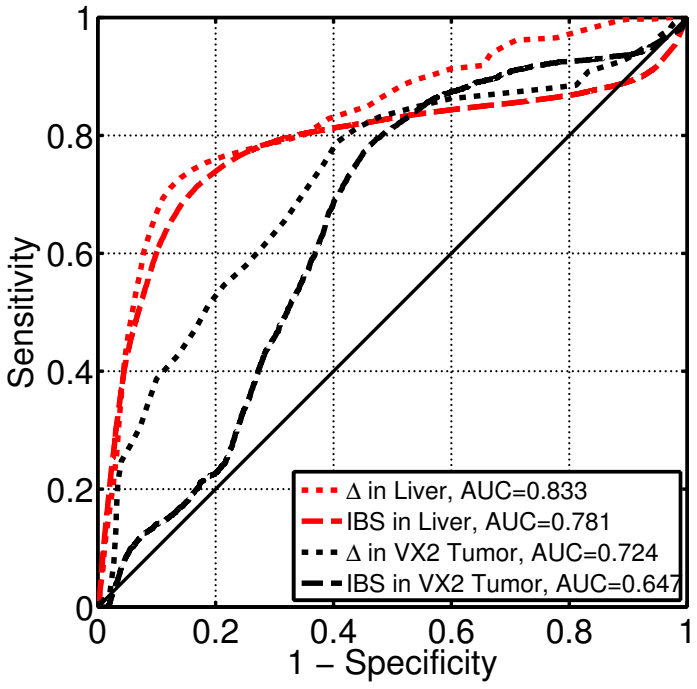

(a)

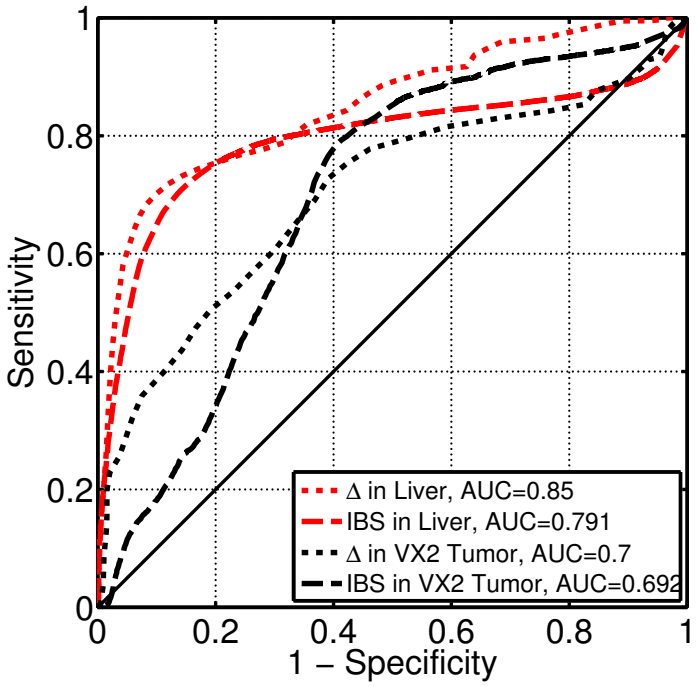

(b)

Figure 2.18: ROC curves illustrating prediction performance for tissue ablation (no TTC uptake) (Figure 2.18a) and tissue treatment (reduced or no TTC uptake) (Figure 2.18b) by corrected echo decorrelation (dotted lines) and IBS (dash–dotted lines) for both exposures in liver (red lines) and VX2 tumor (black lines).

than IBS for focused exposures and for the combined group. For unfocused exposures, IBS predicted ablated regions significantly better than echo decorrelation for ablated regions. In VX2 tumor, there were no significant differences between echo decorrelation and IBS.

	Liver		VX2 tumor	
Exposure	Treated	Ablated	Treated	Ablated
HIFU	2.83 (0.002)	2.51 (0.01)	−0.24 (0.41)	0.11 (0.46)
Bulk	−0.60 (0.27)	−1.81 (0.04)	0.01 (0.50)	0.84 (0.20)
All exposures combined	6.07 ($1{\cdot}10^{-5}$)	4.96 ($1{\cdot}10^{-5}$)	0.18 (0.43)	1.29 (0.10)

Table 2.13: The z–statistic and p–value for comparisons between AUCs for echo decorrelation and IBS ablation prediction of regions of treated and ablated regions in and VX2 tumor.

The optimal thresholds and corresponding sensitivities and specificities for echo decorrelation and IBS are outlined in Table 2.14. At the optimal threshold for prediction of ablated regions, corrected echo decorrelation's sensitivity (TPR) was better than its specificity (1−FPR) for unfocused exposures and focused exposures. For all exposures combined, echo decorrelation's sensitivity was better than its specificity for ablation prediction in VX2 tumor; however, the opposite was observed for ablation prediction in liver. Figure 2.19 illustrates sensitivity and specificity trade offs observed for all exposures combined for $\log_{10}$–scaled echo decorrelation thresholds -12 to -1. For higher thresholds, the specificity is enhanced at the cost of increasingly lower sensitivity. For low thresholds, the sensitivity is enhanced at the cost of increasingly lower specificity.

Figures 2.20a and 2.20b illustrate prediction performance, as measured by the AUC, of echo decorrelation and IBS computed for inter–frame times 8.5, 42.4, 84.7, 127.1, 169.5, 211.9, 254.2, 508.5, and 847.5 ms. Greater AUCs for corrected echo decorrelation in comparison to uncorrected demonstrate performance enhancement by noise correction. An overall decrease in uncorrected and corrected AUC was observed for larger inter–frame times; however, the decrease was less for corrected echo decorrelation. In contrast, IBS AUC was unchanged for

HIFU Ablation	Ablated Normal tissue	Ablated VX2 tumor
Decorrelation optimal threshold	−3.70	−3.20
Sensitivity (TPR)	0.88	0.77
Specificity (1−FPR)	0.81	0.62
IBS optimal threshold	1.82	2.12
Sensitivity (TPR)	0.70	0.75
Specificity (1−FPR)	0.88	0.59
Bulk Ablation		
Decorrelation optimal threshold	−3.10	−3.20
Sensitivity (TPR)	0.70	0.75
Specificity (1−FPR)	0.57	0.60
IBS optimal threshold	3.86	2.98
Sensitivity (TPR)	0.61	0.68
Specificity (1−FPR)	0.69	0.45
All Exposures Combined		
Decorrelation optimal threshold	−3.40	−3.20
Sensitivity (TPR)	0.76	0.76
Specificity (1−FPR)	0.84	0.62
IBS optimal threshold	1.48	2.53
Sensitivity (TPR)	0.74	0.73
Specificity (1−FPR)	0.80	0.58

Table 2.14: Optimal thresholds and the corresponding sensitivity and specificity for corrected echo decorrelation and IBS ablation prediction in liver and VX2 tumor.

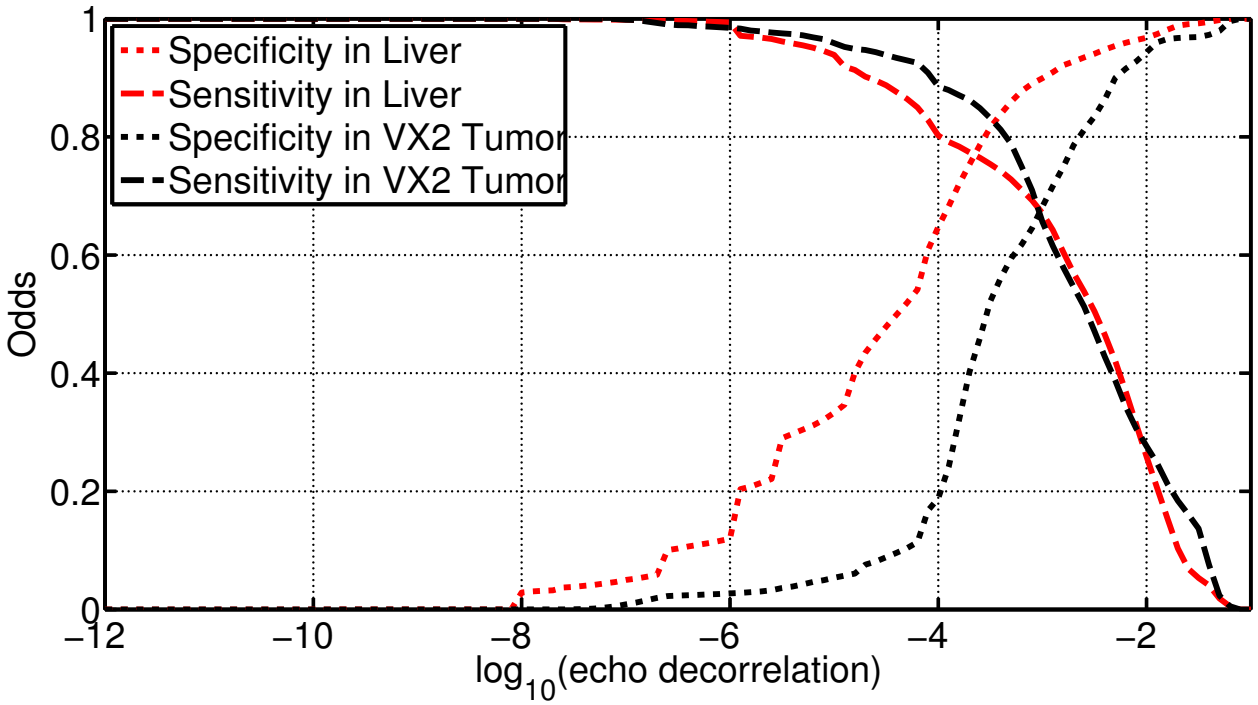

Figure 2.19: $\log_{10}$–scaled echo decorrelation ablation prediction sensitivities (dashed line) and specificities (dotted line) observed for the group of all exposures in liver (red) and VX2 tumor (black).

larger inter–frame times.

2.4 Discussion

Previous echo decorrelation imaging studies have shown promising results for radiofrequency and ultrasound ablation prediction (Mast et al., 2008; Subramanian et al., 2014; Fosnight et al., 2014). The utility and possible limitations of echo decorrelation tumor ablation monitoring in a living subject, where motion could limit echo decorrelation's performance, are discussed below.

Artifactual decorrelation due to tissue displacement and strain/compression caused by respiration, in the context of thermal ablation of liver cancer, and electronic noise can limit ultrasound–based ablation monitoring (Hooi et al., 2015). Table 2.1 illustrates a significant reduction of artifactual echo decorrelation in the non–ablated regions for focused exposures, unfocused exposures, and all exposures combined in liver. Figures 2.20a and 2.20b illustrate that the prediction performance decrease was marginally significant for both focused and unfocused exposures as the inter–frame time increased, possibly indicating an increase of motion–induced decorrelation as previously seen by Subramanian et al. (2014) and Hooi et al. (2015). In contrast, IBS ablation prediction performance decrease for large inter–frame times was insignificant. As IBS is a measure of backscatter energy, as defined in Equation 1.8, the unchanged IBS AUCs seen in Figures 2.20a and 2.20b for greater inter–frame times suggests that the backscatter energy was constant in comparison to echo decorrelation. These results indicate that echo decorrelation and IBS were relatively unaffected by inter–frame times as large as 847.5 ms for this *in vivo* model.

The ROC results illustrated in Figures 2.16, 2.17, and 2.18 indicate that echo decorrelation imaging is a successful predictor of local ablation. In liver, echo decorrelation and integrated backscatter (IBS) prediction performance was significantly better than chance

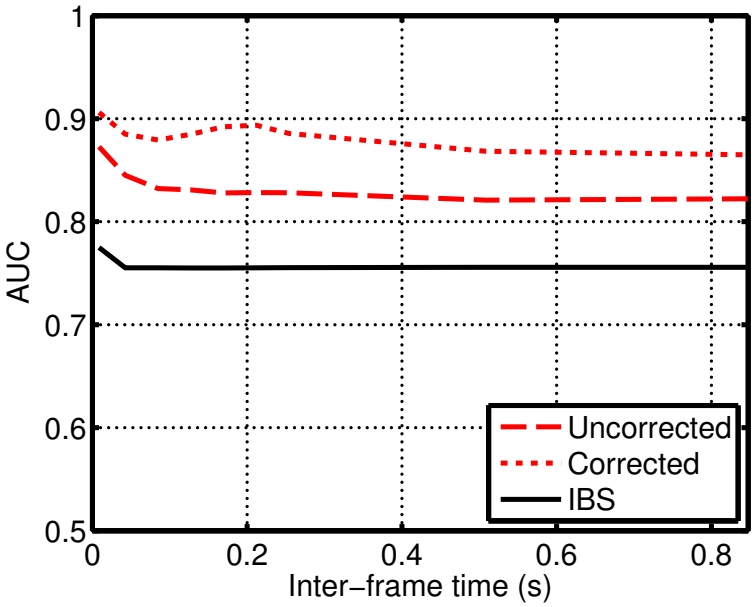

(a)

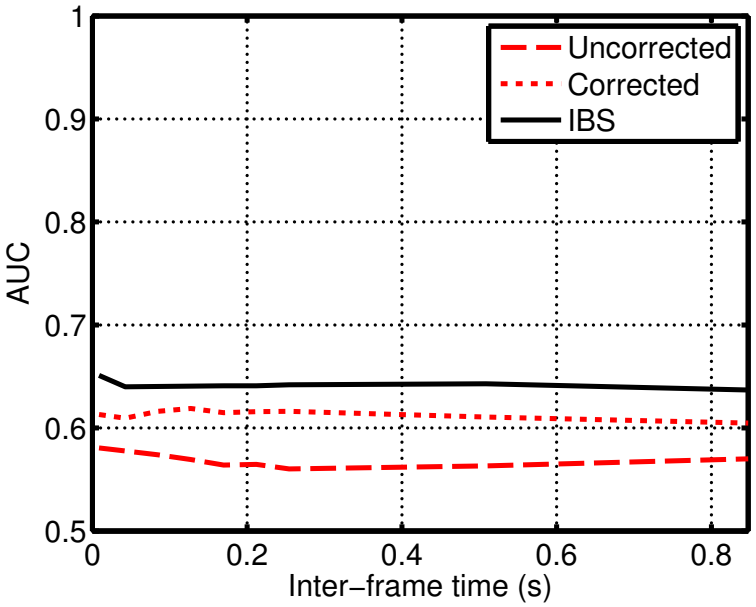

(b)

Figure 2.20: AUCs for uncorrected (red–dash line) and corrected (red–dotted line) echo decorrelation and IBS (black–solid line) computed for τ (inter–frame time) = 8.5, 42.4, 84.7, 127.1, 169.5, 211.9, 254.2, 508.5, and 847.5 ms. Ablation prediction performance was tested for focused (a) and unfocused (b) exposures in liver.

(AUC=0.5) (Tables 2.9 and 2.10). In tumor, echo decorrelation and IBS predicted tumor ablation significantly better than chance for all exposures combined (Tables 2.11 and 2.12). For the unfocused exposures and focused exposures, AUC values for tumor were insignificant or marginally significant, consistent with marginal differences between echo decorrelation in ablated and non–ablated tumor (Figures 2.13, 2.14a, and 2.15a). The lower statistical significance is in part due to the smaller number of predictions in tumor in comparison to the number of predictions in liver.

Ablation prediction in liver by echo decorrelation was significantly more successful than prediction by IBS for the focused exposures and for all exposures combined, consistent with previous observations (Mast et al., 2008; Subramanian et al., 2014; Fosnight et al., 2014). This result implies echo decorrelation imaging can predict ablation better than conventional B–mode (brightness–mode) ultrasound imaging, as image brightness is proportional to the echo amplitude (Szabo et al., 2004). However, for the unfocused exposure group, IBS predicted ablated liver significantly better than echo decorrelation. Echo decorrelation did not predict ablated VX2 tumor significantly better than IBS for the focused exposures, unfocused exposures, or for all exposures combined.

Differences in echo decorrelation in liver and tumor were seen for the unfocused group. There was a trend of lower decorrelation in ablated tumor than in ablated liver (Figure 2.14); however, these differences were not significant (Table 2.4 and 2.7). This result is additionally highlighted by sub–figures 2.5 Q, R and T, where the log–scaled echo decorrelation is generally lower in ablated tumor regions in comparison to ablated liver. This trend may be due to the content and/or structure of the tumor tissue as a result of tumor size. For a VX2 rabbit liver cancer model, Wu et al. (2009) observed necrosis development in the tumor center, thickening of the tumor border, and a increased blood stasis in the tumor rim as tumor size increased. These changes may lead to varying micro–structural changes during thermal ablation. This implies that tumor heating and/or echo decorrelation's ablation prediction

performance may depend on the size of the VX2 tumor.

Echo decorrelation's 2.35 mm spatial resolution for a window size of 1 mm, determined using Equation (2.8), might explain the insignificant differences between decorrelation in non–ablated vs. ablated regions observed for focused exposures, unfocused exposures, and all exposures combined in VX2 tumor. Hooi et al. (2015), using simulated echo decorrelation images, showed that a correlation window size approximately 1/6 the expected lesion size was most appropriate. For these experiments, the 1.00 mm window size was thus appropriate for unfocused ablation (the approximate optimal window size, estimated from the Gaussian beam models of Section 2.2.4, is 1.67 mm) but suboptimal for focused ablation (approximate optimal window size 0.02 mm). For accurate imaging of focused ablation, improved echo decorrelation performance could be achieved using a smaller correlation window size. To this end, the pulse–echo image resolution must also be improved. Improved pulse–echo imaging is achieved by utilizing more transmit imaging foci or increasing the imaging center frequency, the transducer bandwidth, and/or the active aperture size (Szabo et al., 2004); however, improved resolution will increase motion–induced decorrelation.

Another cause of poor prediction is lesion motion during treatment. Lesion movement might lead to high false positive rates (i.e., low ablation contrast). The ablation prediction performance for focused exposures would be more affected in comparison to the unfocused exposures due to the larger ablated region.

These results indicate echo decorrelation imaging is a successful predictor of local ablation, with potential for real–time ultrasound system implementation and successful clinical translation. For most cases, echo decorrelation predicted ablated liver better than IBS and predicted ablated VX2 tumor marginally better than IBS. Tissue motion effects were shown to have little effect on echo decorrelation's ablation prediction performance; however, focused ablation prediction performance could potentially be enhanced by improving pulse–echo image resolution. Additionally, enhancement of prediction performance could be achieved by

leveraging three–dimensional volume ultrasound imaging systems, which inherently have slower frame rates, as echo decorrelation's performance was marginally affected by tissue motion. These results suggest that echo decorrelation imaging merits further investigation and has potential to improve real–time monitoring during HIFU thermal ablation and bulk ultrasound thermal ablation.

Chapter III

Conclusions

3.1 Summary

An unmet need of thermal ablation is real time mapping of heat–induced cell death (Li et al., 2014). To this end, echo decorrelation imaging is currently being studied as a ultrasound–based method for real time thermal ablation guidance and monitoring.

The central hypothesis of this study was that ultrasound echo decorrelation accurately predicts *in vivo* ultrasound thermal ablation. To test this hypothesis, *in vivo* pulse–echo imaging of high–intensity focused ultrasound (HIFU) and bulk ultrasound thermal ablation were performed on rabbit liver and VX2 tumor. The prediction performance of echo decorrelation and integrated backscatter (IBS) was determined by comparing the parameter maps to triphenyl tetrazolium chloride (TTC) stained histology and computing the receiver operating characteristic (ROC) curve.

The central hypothesis of this study was confirmed for focused exposures, unfocused exposures, and all exposures combined, in both normal liver and VX2 tumor for echo decorrelation. For the focused exposures, unfocused exposures, and all exposures combined, ablated normal liver was predicted significantly better by echo decorrelation than IBS. For the focused exposures, unfocused exposures, and all exposures combined, ablated VX2 tumor

was not predicted significantly better by echo decorrelation in comparison to IBS. Analysis of inter–frame time effects illustrated a marginally significant decrease in prediction performance by echo decorrelation for large tissue motion.

These results suggest that echo decorrelation imaging merits further investigation and has potential to improve liver cancer ablation outcomes. In addition to liver cancer thermal ablation, echo decorrelation imaging could also improve outcomes for other emerging thermal ablation cancer therapies for breast tumors, pancreatic cancer, kidney tumors, thyroid and parathyroid tumors (Maloney et al., 2015). Ultrasound guided HIFU (USgHIFU) and magnetic resonance imaging guided HIFU (MRgHIFU) systems have been used to safely guide HIFU therapy for these soft tissue cancers (Maloney et al., 2015). The deployment of these imaging technologies indicates a need for real time image monitoring, for which echo decorrelation imaging could provide a relatively low cost and less complex solution.

Echo decorrelation imaging could also improve outcomes for emerging non–cancer thermal ablation therapies. These include thermal therapies for the heart (e.g., atrial fibrillation, ventricular tachycardia, and transmyocardial revascularization therapies) (O'Reilly et al., 2015; Salgaonkar et al., 2015) and thermal sympathetic nerve modulation for hypertension (Shetty et al., 2015). ProRhythm (Ronkonkoma, NY), formerly Transurgical, (Schmidt et al, 2007) and Atrionix Inc. (Natale et al., 2000) have developed transballoon ultrasound ablation catheters for atrial fibrillation therapy and both saw positive results in initial human studies. Symplicity (Medtronic, Palo Alto, CA, USA), the Therapeutic Intra Vascular Ultrasound (TIVUS) System developed by Cadriosonic Ltd (Tel Aviv, Israel) and the PARADISE (ReCor Medical, Ronkonkoma, NY, USA) system, which has received the CE–mark, have been developed for thermal sympathetic nerve modulation (Shetty et al., 2015). The TIVUS and PARADIS systems leverage non–focused ultrasound thermal ablation (i.e., bulk ultrasound thermal ablation) approaches (Shetty et al., 2015) where as Symplicity leverages radiofrequency energy (Shetty et al., 2015). Ablation efficacy could be improved by deploy-

ing echo decorrelation imaging. Currently, these approaches do not have methods to monitor ablation directly (Shetty et al., 2015; O'Reilly et al., 2015; Salgaonkar et al., 2015).

3.2 Future directions

An important next step is assessing echo decorrelation ability to successfully control ablation in real time. Control by echo decorrelation would be assessed in a series of *in vitro* studies where corrected echo decorrelation images would be computed in real time from pulse–echo images of *in vitro* HIFU and bulk ultrasound ablation in bovine liver. Treatment could be terminated when the local mean or maximum $\log_{10}$–scaled echo decorrelation anywhere within the planned treatment zone reaches an optimal threshold. The threshold for ablation control should be designed to achieve at least a specificity of 90%, thus potentially decreasing the odds of local recurrence; however, the cost will be lower sensitivity. To achieve a 90% specificity, Figure 2.19 indicates the optimal threshold for ablated liver and VX2 tumor prediction by $\log_{10}$–scaled echo decorrelation would be -2.9 and -2.3 respectively. The sensitivities at these thresholds would be 0.65 and 0.43 for ablated liver and VX2 tumor prediction. Preliminary verifications would demonstrate total treatment zone ablation after therapy termination. After initial verification *in vitro*, additional *in vivo* studies would be conducted to assess *in vivo* HIFU and bulk ultrasound ablation control.

An additionally important next step is translation of real time ultrasound echo decorrelation imaging monitoring into clinical radiofrequency ablation (RFA) to assess echo decorrelation's ablation prediction performance in realistic liver tissue (e.g., inflamed, cirrhotic, and fatty infiltrated liver).

Echo decorrelation imaging is expected to successfully predict thermal ablation in a clinical setting, as echo decorrelation is believed to map thermal–induced tissue micro–structural changes as well as transient gas activity (Hooi et al., 2015). These micro–structural changes

are believed to be due to cellular swelling, microvascular changes, protein denaturation, and microstructural tissue damage due to water vaporization during thermal ablation (Gravante et al., 2011). These processes can involve changes in proteins, which serve as the structural molecule of all cells (O'Connor et al., 2010), or water vaporization. Additionally, microstructural changes of saturated fatty acids are expected at their approximate melting temperature (43–69 °C) (Timberlake et al., 2014). As liver tissues are primarily composed of these molecules, echo decorrelation imaging is hypothesized to predict thermal ablation even in the presence of liver tissue abnormalities like inflammation, liver cirrhosis, and fatty infiltrations.

Echo decorrelation images could be computed from pulse–echo images acquired during clinical RFA and compared to follow–up CT images (computed tomography), MR (magnetic resonance) images, post–surgical biopsies, or simulated RFA lesions to assess echo decorrelation's ablation prediction performance during abnormal liver ablation. Ultrasound probe position sensors would allow accurate registration of echo decorrelation images with a surrogate tissue ablation map, as done by Mauri et al. (2015) for B–mode (brightness mode) and CT/MRI registration.

Echo decorrelation could be computed from two–dimensional pulse–echo images for experimental simplicity. However, volume (i.e., three–dimensional) ultrasound imaging technologies could be leveraged for enhanced monitoring as thermal ablation is intrinsically three–dimensional. Volume ultrasound imaging has previously been deployed for liver tumor targeting and RFA treatment planning (i.e., tumor dimensioning, RFA needle selection, and needle placement) and was found superior to two–dimensional ultrasound imaging (Kunzli et al., 2011). Ablated zones mapped by echo decorrelation imaging would further enhance treatment planning such as RFA needle electrode selection and the placement of a single or a combination of electrodes (Kunzli et al., 2011). These procedural advancements could increase the ablated zone diameters to as large as 7 cm (Kunzli et al., 2011). Enhanced

planning would overall result in lower local recurrence rates for both smaller tumors (2 to 3 cm in diameter; recurrence rate 21.6%) and larger tumors (>3 cm in diameter; recurrence rate 52.8%; (Kunzli et al., 2011).

These important next steps would demonstrate echo decorrelation imaging's clinical translatability and efficacy in monitoring thermal ablation of liver and other soft tissue cancers (e.g., breast tumors, pancreatic cancer, kidney tumors, thyroid and parathyroid tumors). Efficacy of non–cancer therapies such as treatments for the heart (e.g., atrial fibrillation, ventricular tachycardia, and transmyocardial revascularization therapies) and thermal sympathetic nerve modulation for hypertension could also be improved by this novel ultrasound–based approach.

Chapter IV

Appendix

Trial #	Rabbit ID #	On time (s)	Off time (s)	Cycles	A.P.O. (W)	Voltage (V)	Energy Abs. (J)	F_{depth} (mm)	Aperture	P_{gain}	ISPTP (W/cm^2)
Date: 1/27/2014	Array: THX5A JV815	f_c: 5.00 MHz									
1	R252 / Middle lobe	7.5	5.5	6	39	14.70	1755	∞	1-64	1.43	68
2	R252 / Right lobe	7.5	5.5	6	24	10.56	1080	∞	1-64	1.43	42
3	R252 / Left lobe	7.5	5.5	6	32	12.70	1440	∞	1-64	1.43	56
1	R253 / Left lobe	1	5	6	25	10.70	150	36.00	1-64	4.86	505
2	R253 / Middle lobe	1	5	6	21	8.86	126	36.00	1-64	4.86	424
3	R253 / Right lobe	1	5	6	25	10.70	150	36.00	1-64	4.86	505
Date: 4/29/2014	Array: THX5A SN004	f_c: 5.20 MHz									
1	R256 / Right lobe	1	5	6	22	9.23	132	30.00	1-64	6.52	800
2	R256 / Middle lobe	1	5	6	26	10.21	156	30.00	1-64	6.52	945
^{N}3	R256 / Left lobe	7.5	5	6	35	12.49	1575	∞	100	1.44	50
^{O}4	R259 / Right lobe	7.5	5	6	28	10.70	1260	∞	100	1.44	62
5	R259 / Middle lobe	1	5	6	30	11.15	180	30.00	1-64	6.52	1091
6	R259 / Middle lobe	1	5	6	30	11.50	180	30.00	1-64	6.52	1091
7	R259 / Left lobe	1	5	6	35.4	12.50	212	30.00	1-64	6.52	1287
8	R259 / Left lobe	1	5	6	35.4	12.50	212	30.00	1-64	6.52	1287
Date: 7/2/2014	Array: THX5A SN003	f_c: 5.05 MHz									
1	R265 / Left lobe	6	2.5	9	25	10.70	1350	∞	1-32	1.45	45
2	R265 / Middle lobe	6	2.5	9	29.17	11.80	1575	∞	1-32	1.45	52
3	R265 / Right lobe	6	2.5	7	33.03	13.00	1387	∞	1-32	1.45	59
4	R266 / Left lobe	0.7	3.3	9	28.6	11.60	180	30.00	1-64	6.58	1057
5	R266 / Middle lobe	0.7	3.3	9	23.8	10.50	150	30.00	1-64	6.58	880
^{A}6	R266 / Right lobe	0.7	3.3	9	23.8	10.50	150	27.00	1-64	7.29	1080
Date: 11/17/2014	Array: THX5A SN007	f_c: 5.00 MHz									
^{P}1	R267 / Left lobe	6	2.5	9	30	12.00	1620	∞	1-64	1.43	52
^{B}2	R267 / Middle lobe	0.7	3.3	9	24	10.50	151	25.00	1-64	7.64	1196
3	R267 / Right lobe	0.7	3.3	9	28	11.50	176.40	27	1-64	7.34	1287
^{C}4	R267 / Right lobe	0.7	3.3	9	28	11.50	176	28.00	1-64	7.14	1220
^{D}5	R268 / Left lobe	0.7	3.3	9	28	11.50	176	26.00	1-64	7.51	1351
6	R268 / Right lobe	6	2.5	9	30	12.00	1620	∞	1-64	1.43	52
^{E}7	R268 / Middle lobe	0.7	3.3	9	24	10.50	151	27.00	1-64	7.34	1103
^{F}8	R268 / Middle lobe	0.7	3.3	9	24	10.50	151	25.00	1-64	7.64	1196

Table 4.1: Exposures for all *in vivo* experiments. Superscript letters denote trials analyzed in this thesis (Figures 2.5). For each experiment day, the linear image-ablate array identification number and center frequency are listed. For each trial, the rabbit identification number, liver lobe, sonication time, rest time, number of sonication pulses, acoustic power output (APO) and its calibrated voltage, total energy absorbed, electronic focal depth, the percent of the available active aperture used, pressure gain determined from simulations (Mast et al., 2007), and spatial peak-temporal peak *in situ* intensity are listed.

Trial #	Rabbit ID #	On time (s)	Off time (s)	Cycles	A.P.O. (W)	Voltage (V)	Energy (J)	F_{depth} (mm)	Aperture	P_{gain}	ISPTP (W/cm^2)
Date: 12/17/2014	Array: THX5A SN007	f_c: 5.00 MHz									
1	R269 / Left lobe	0.7	2.8	9	28	11.50	176	∞	1-64	1.43	47
^{Q}2	R269 / Middle lobe	6	2.5	9	35	13.12	1890	∞	100	1.43	61
3	R269 / Right lobe	0.7	2.8	9	24	10.36	151	∞	1-64	1.43	42
3 (left mark)	R269 / Right lobe	6.5	2.5	7	34	13.00	1547	∞	1-10	1.43	59
3 (right mark)	R269 / Right lobe	6.5	2.5	6	34	13.00	1326	∞	55-64	1.43	59
^{R}4	R270 / Left lobe	6	2.5	9	30	11.72	1620	∞	1-64	1.43	52
5	R270 / Middle lobe	0.7	2.8	9	28	11.50	176	∞	1-64	1.43	49
5 (left mark)	R270 / Middle lobe	6.5	2.5	10	34	13.00	2210	∞	1-10	1.43	59
5 (right mark)	R270 / Middle lobe	6.5	2.5	9	34	13.00	1989	∞	55-64	1.43	59
^{S}6	R270 / Right lobe	6	2.5	8	35	13.12	1680	∞	1-64	1.43	61
7	R270 / Right lobe	0.7	3.3	9	28	11.50	176	∞	1-64	1.43	59
8	R270 / Left lobe	0.7	3.3	9	28	11.50	176	∞	1-64	1.43	59
Date: 2/4/2015	Array: THX5A SN913	f_c: 5.40 MHz									
^{T}1	R271 / Middle lobe	6	2.5	9	30	13.20	1620	∞	1-64	1.45	54
^{G}2	R271 / Left lobe	0.7	2.8	9	24	11.24	151	24.00	1-64	7.10	1033
2 (left mark)	R271 / Left lobe	6	2.5	5	33	14.00	990	∞	1-10	1.45	59
2 (right mark)	R271 / Left lobe	6	2.5	3	33	14.00	594	∞	55-64	1.45	59
3	R271 / Right lobe	0.7	2.8	9	20	10.06	126	26.00	1-64	7.30	911
^{H}4	R272 / Left lobe	0.7	2.8	9	28	12.50	176	23.00	1-64	6.66	1061
4 (left mark)	R272 / Left lobe	6	2.5	6	33	14.00	1188	∞	1-10	1.45	59
4 (right mark)	R272 / Left lobe	6	2.5	10	33	14.00	1980	∞	55-64	1.45	59
^{I}5	R272 / Middle lobe	0.7	2.8	9	20	10.06	126	26.00	1-64	7.30	911
^{J}6	R272 / Right lobe	0.7	2.8	9	24	11.24	151	24.00	1-64	7.10	1033
^{K}7	R272 / Left lobe	0.7	3.3	9	24	11.24	151	24.00	1-64	7.10	1033
Date: 3/23/2015	Array: THX5A SN913	f_c: 5.40 MHz									
^{U}1	R273 / Middle lobe	6	2.5	7	35	14.00	1470	∞	1-64	1.45	63
2	R273 / Left lobe	0.7	2.8	6	28	12.51	118	25.00	1-64	7.35	1292
2 (left mark)	R273 / Left lobe	6	2.5	10	33	14.00	1980	∞	1-10	1.45	59
2 (right mark)	R273 / Left lobe	6	2.5	6	33	14.00	1980	∞	55-64	1.45	59
^{L}3	R273 / Right lobe	0.7	2.8	6	24	11.24	101	25.00	1-64	7.35	1107
3 (left mark)	R273 / Right lobe	6	2.5	5	33	14.00	990	∞	1-10	1.45	59
3 (right mark)	R273 / Right lobe	6	2.5	10	33	14.00	1980	∞	55-64	1.45	59
^{V}1	R274 / Left lobe	6	2.5	8	30	13.12	1440	∞	1-64	1.45	54
^{W}2	R274 / Middle lobe	6	2.5	9	35	14.00	1890	∞	1-64	1.45	63
^{M}3	R274 / Right lobe	0.7	2.8	9	28	12.15	176	25.00	1-64	7.35	1292
3 (left mark)	R274 / Right lobe	6	2.5	4	33	14.00	792	∞	1-10	1.45	59
3 (right mark)	R274 / Left lobe	6	2.5	10	33	14.00	1980	∞	55-64	1.45	59

Table 4.1 continued.

Trial #	Iris B–scan before thx	Iris B–scan after thx	Filename (sham)	Filename (thx)	Max. tumor dia.
Date: 1/27/2014	Array: THX5A JV815	f_c: 5.00 MHz			
1	12:11:31	12:11:05	NA	NA	no tumor
2	12:31:39	12:31:28	NA	01272014_111619	6.0
3	12:41:44	12:48:32	01272014_112813	01272014_113014	no tumor
1	12:41:44	12:48:24	01272014_125927	01272014_130111	no tumor
2	2:15:13	2:18:27	01272014_132311	01272014_132517	no tumor
3	2:59:47	3:05:44	01272014_133915	01272014_134446	3.1
Date: 4/29/2014	Array: THX5A SN004	f_c: 5.20 MHz			
1	8:59:00	9:03:00	04292014_185927	04292014_090142	11.5
2	9:10:00	9:14:00	04292014_091019	04292014_091305	no tumor
$^{N}3$	9:25:00	9:36:00	04292014_092757	04292014_093434	11.0
$^{O}4$	10:50:00	11:05:00	04292014_105943	04292014_110305	11.1
5	11:26:00	11:33:00	04292014_112810	04292014_113148	13.6
6	11:40:00	11:43:00	04292014_114050	04292014_114220	no tumor
7	11:50	11:54	04292014_115020	04292014_115311	9.2
8	11:59	12:03	04292014_120000	04292014_120140	no tumor
Date: 7/2/2014	Array: THX5A SN003	f_c: 5.05 MHz			
1	8:46:00	8:52:00	07022014_084549	07022014_084853	no tumor
2	9:15:00	9:20:00	07022014_091429	07022014_091710	no tumor
3	9:32:00	9:42:00	07022014_093410	07022014_093706	tumor
4	11:27:00	11:33:00	07022014_112942	07022014_113112	no tumor
5	11:48:00	12:07:00	07022014_114739	07022014_115307	no tumor
$^{A}6$	12:18:00	12:26:00	07022014_122208	07022014_122407	no tumor
Date: 11/17/2014	Array: THX5A SN007	f_c: 5.00 MHz			
$^{P}1$	8:11:00	8:19:00	11172014_092824	11172014_092824	5.1
$^{B}2$	8:34:00	8:35:00	11172014_094831	11172014_094831	6.0
3	8:49:00	8:52:00	11172014_100331	11172014_100331	7.8
$^{C}4$	9:01:00	9:04:00	11172014_101503	11172014_101503	no tumor
$^{D}5$	10:10:00	10:15:00	11172014_112547	11172014_112547	5.4
6	10:29:00	10:33:00	11172014_114239	11172014_114239	10.6
$^{E}7$	10:38	10:40	11172014_115127	11172014_115127	no tumor
$^{F}8$	10:43	10:46	11172014_115719	11172014_115719	no tumor

Table 4.2: Time stamps of B–scans taken with the Iris system before and after treatment, the raw pulse-echo data filename, and effective tumor diameters were recorded for each experiment.

Trial #	Iris B–scan before thx	Iris B–scan after thx	Filename (sham)	Filename (thx)	Max. tumor dia.
Date: 12/17/2014	Array: THX5A SN007	f_c: 5.00 MHz			
1	7:28:00	7:27:00	12172014_084053	12172014_084053	no tumor
$^{Q}2$	7:52:00	7:55:00	12172014_090453	12172014_090453	10.1
3	8:06:00	8:08:00	12172014_091846	12172014_091846	no tumor
3 (left mark)	NA	8:13:00	12172014_092247	12172014_092247	NA
3 (right mark)	NA	8:19:00	12172014_092812	12172014_092812	NA
$^{R}4$	9:12:00	9:16:00	12172014_102531	12172014_102531	3.5
5	9:22:00	9:25:00	12172014_103634	12172014_103634	no tumor
5 (left mark)	NA	9:30:00	12172014_103855	12172014_103855	NA
5 (right mark)	NA	9:33:00	20141217_104310	20141217_104310	NA
$^{S}6$	9:49:00	9:53:00	12172014_110242	12172014_110242	5.3
7	9:59	10:03	12172014_111425	12172014_111425	no tumor
8	10:16	10:19	12172014_112937	12172014_112937	no tumor
Date: 2/4/2015	Array: THX5A SN913	f_c: 5.40 MHz			
$^{T}1$	8:47:00	8:54:00	02042015_084822	02042015_084822	3.5
$^{G}2$	9:09:00	9:14:00	02042015_091009	02042015_091009	7.7
2 (left mark)	NA	9:22:00	02042015_091555	02042015_091555	NA
2 (right mark)	NA	9:28:00	02042015_092217	02042015_092217	NA
3	9:38:00	9:41:00	02042015_093710	20402015_093710	no tumor
$^{H}4$	11:01:00	11:07:00	02042015_110338	02042015_110338	8.1
4 (left mark)	NA	11:12:00	02042015_110642	02042015_110642	NA
4 (right mark)	NA	11:16:00	02042015_111012	02042015_111012	NA
$^{I}5$	11:29:00	11:32:00	02042015_112841	02042015_112841	no tumor
$^{J}6$	11:46:00	11:48:00	02042015_114410	02042015_114410	no tumor
$^{K}7$	11:58	12:00	02042015_115645	02042015_115645	no tumor
Date: 3/23/2015	Array: THX5A SN913	f_c: 5.40 MHz			
$^{U}1$	7:35:00	7:42:00	03232015_083552	03232015_083552	no tumor
2	7:52:00	7:57:00	03232015_085211	03232015_085211	12.0
2 (left mark)	7:58:00	8:01:00	20150323_090728	20150323_090728	NA
2 (right mark)	8:01:00	8:18:00	NA	NA	NA
$^{L}3$	8:34	8:38:00	03232015_093232	03232015_093232	9.8
3 (left mark)	NA	8:44:00	03232015_093722	03232015_093722	NA
3 (right mark)	8:44	8:48:00	03232015_094144	03232015_094144	NA
$^{V}1$	10:13:00	10:17:00	03232015_111056	03232015_111056	no tumor
$^{W}2$	10:30:00	10:33:00	03232015_112703	03232015_112703	8.5
$^{M}3$	10:40:00	11:43:00	03232015_113758	03232015_113758	14.4
3 (left mark)	NA	10:47	03232015_114042	03232015_114042	NA
3 (right mark)	10:47	11:47	03232015_114417	03232015_114417	NA

Table 4.2 continued.

Bibliography

Aubry, J. F., Pauly, K., Moonen, C., ter Haar, G., Ries, M., Salomir, R., Sokka, S., Sekins, K. M., Shapira, Y., Ye. F., Huff-Simon, H., Eames, M., Hananel, A., Kassell, N., Napoli, A., Hwang, J. H., Wu, F., Zhang, L., Melzer, A., Kim, Y., and Gedroyc, W. M. (2013). The road to clinical use of high-intensity focused ultrasound for liver cancer: technical and clinical consensus. Journal of Therapeutic Ultrasound, 1(13), pp. 1-7.

Barthe, P. G., Slayton, M. H., Jaeger, P. M., Makin, I. R. S., Gallagher, L. A., Mast, T. D., Runk, M. M., and Faid, W. (2004). Ultrasound therapy system and ablation results utilizing miniature imaging/therapy arrays. Proceedings of the 2004 IEEE Ultrasonics Symposium, 3, pp. 1792-1795.

Brace, C. L. (2009). Radiofrequency and microwave ablation of the liver, lung, kidney, and bone: what are the differences? Current Problems in Diagnostic Radiology, 38(3), pp. 135-143.

Breen, D. J., and Lencioni, R. (2015). Image-guided ablation of primary liver and renal tumors. Nature Reviews Clinical Oncology, 12(3), pp. 175-186.

Bruix, J., and Sherman, M. (2005). Management of hepatocellular carcinoma. Hepatology, 42(5), pp. 1208-1236.

Bruix, J., and Sherman, M. (2011). Management of hepatocellular carcinoma: an update. Hepatology, 53(3), pp. 1020-1022.

Carrafiello, G., Laganà, D., Mangini, M., Fontana, F., Dionigi, G., Boni, L., and Fugazzola, C. (2008). Microwave tumors ablation: principles, clinical applications and review of preliminary experiences. International Journal of Surgery, 6, pp. S65-S69.

Cespedes, I., Ophir, J., and Alam, S. K. (1997). The combined effect of signal decorrelation and random noise on the variance of time delay estimation. IEEE Transactions on Ultrasonics, Ferroelectrics, and Frequency Control, 44(1), pp. 220-225.

Chen, W. H., Sanghvi, N. T., Carlson, R., Schatzl, G., Marberger, M., Muratore, R., and Konofagou, E. E. (2012). Validation of tissue change monitoring (TCM) on the Sonablate® 500 during high intensity focused ultrasound (HIFU) treatment of prostate cancer with real-time thermometry. In AIP Conference Proceedings-American Institute of Physics, 1481(1), pp. 53).

DeLong, E. R., DeLong, D. M., and Clarke-Pearson, D. L. (1988). Comparing the areas under two or more receiver operating characteristic curves: a nonparametric approach. Biometrics, 44(3), pp. 837-845.

Diederich, C. J., Nau, W. H., and Stauffer, P. R. (1999). Ultrasound applicators for interstitial thermal coagulation. IEEE Transactions on Ultrasonics, Ferroelectrics, and Frequency Control, 46(5), pp. 1218-1228.

Focused Ultrasound Foundation (2015). Focused Ultrasound State of the Field 2015, p. 46. Retrieved from http://fusfoundation.org/images/pdf/State_of_the_field_2015.pdf.

Fosnight, T. R., Hooi, F. M., Colbert, S. B., Keil, R. D., Barthe, P. G., and Mast, T. D. (2014). Echo decorrelation imaging of ex vivo HIFU and bulk ultrasound ablation

using image-treat arrays. 14th International Symposium on Therapeutic Ultrasound, AIP Conference Proceedings.

Fosnight, T. R., Hooi, F. M., Keil, R. D., Subramanian, S., Barthe, P. G., Wang, Y., Ren X., Ahmad S., Rao M.B., and Mast, T. D. (2014). Motion-corrected echo decorrelation imaging of in vivo focused and bulk ultrasound ablation in a rabbit liver cancer model. Proceedings of the 2014 IEEE Ultrasonics Symposium, pp. 2161-2164.

Goldberg, S. N. (2001). Radiofrequency tumor ablation: principles and techniques. European Journal of Ultrasound, 13(2), pp. 129-147.

Gravante, G., Ong, S. L., Metcalfe, M. S., Bhardwaj, N., Lloyd, D. M., and Dennison, A. R. (2011). The effects of radiofrequency ablation on the hepatic parenchyma: Histological bases for tumor recurrences. Surgical Oncology, 20(4), pp. 237-245.

Hanley, J. A., and McNeil, B. J. (1982). The meaning and use of the area under a receiver operating characteristic (ROC) curve. Radiology, 143(1), pp. 64-71.

Hooi, F. M., Nagle, A., Subramanian, S., and Mast, T. D. (2015). Analysis of tissue changes, measurement system effects, and motion artifacts in echo decorrelation imaging. Journal of the Acoustical Society of America, 137(2), pp. 585-597.

Karunakaran, Chandrapriya. "Role of Cavitation during Bulk Ultrasound Ablation: Ex vivo and In vivo Studies." Ph.D. Dissertation. University of Cincinnati, 2012.

Kennedy, J. E., ter Haar, G. R., and Cranston, D. (2003). High intensity focused ultrasound: surgery of the future? British Journal of Radiology, 76(909), pp. 590-599.

Kolokythas, O., Gauthier, T., Fernandez, A. T., Xie, H., Timm, B. A., Cuevas, C., Dighe, M. K., Mitsumori, L. M., Bruce, M. F., Herzka, D. A., Goswami, G. K., Andrews, R. T., Oas, K. M., Dubinsky, T. J., and Warren, B. H.(2008). Ultrasound-based elastography: A novel

approach to assess radio frequency ablation of liver masses performed with expandable ablation probes: a feasibility study. Journal of Ultrasound in Medicine, 27(6), pp. 935-946.

Krzanowski, W. J., and Hand, D. J. (2009). ROC Curves for Continuous Data (Chapman and Hall/CRC Press), Ch. 9, pp. 172-175.

Kunzli, B. M., Abitabile, P., and Maurer, C. A. (2011). Radiofrequency ablation of liver tumors: Actual limitations and potential solutions in the future. World Journal of Hepatology, 3(1), pp. 8.

Lafon, C., de Lima, D. M., Theillere, Y., Prat, F., Chapelon, J. Y., and Cathignol, D. (2002). Optimizing the shape of ultrasound transducers for interstitial thermal ablation. Medical Physics, 29(3), pp. 290-297.

Li, D., Kang, J., and Madoff, D. C. (2014). Locally ablative therapies for primary and metastatic liver cancer. Expert Review of Anticancer Therapy, 14(8), pp. 931-945.

Liu, D., and Ebbini, E. S. (2010). Real-time 2-D temperature imaging using ultrasound. IEEE Transactions on Biomedical Engineering, 57(1), pp. 12-16.

Makin, I. R. S., Mast, T. D., Faidi, W., Runk, M. M., Barthe, P. G., and Slayton, M. H. (2005). Miniaturized ultrasound arrays for interstitial ablation and imaging. Ultrasound in Medicine and Biology, 31(11), pp. 1539-1550.

Maloney, E., and Hwang, J. H. (2015). Emerging HIFU applications in cancer therapy. International Journal of Hyperthermia, 31(3), pp. 302-309.

Maruyama, H., Yoshikawa, M., and Yokosuka, O. (2008). Current role of ultrasound for the management of hepatocellular carcinoma. World Journal of Gastroenterology, 14(11), pp. 1710-1719.

Mast, T. D., Makin, I. R. S., Faidi, W., Runk, M. M., Barthe, P. G., and Slayton, M. H. (2005). Bulk ablation of soft tissue with intense ultrasound: Modeling and experiments. Journal of the Acoustical Society of America, 118(4), pp. 2715-2724.

Mast, T. D. (2007). Fresnel approximations for acoustic fields of rectangularly symmetric sources. Journal of the Acoustical Society of America, 121(6), pp. 3311-3322.

Mast, T. D., Pucke, D. P., Subramanian, S. E., Bowlus, W. J., Rudich, S. M., and Buell, J. F. (2008). Ultrasound monitoring of in vitro radio frequency ablation by echo decorrelation imaging. Journal of Ultrasound in Medicine, 27(12), pp. 1685-1697.

Mast, T. D., Barthe, P. G., Makin, I. R. S., Slayton, M. H., Karunakaran, C. P., Burgess, M. T., Alqadah A., and Rudich, S. M. (2011). Treatment of rabbit liver cancer in vivo using miniaturized image-ablate ultrasound arrays. Ultrasound in Medicine and Biology, 37(10), pp. 1609-1621.

Mauri, G., Cova, L., De Beni, S., Ierace, T., Tondolo, T., Cerri, A., Goldberg, N., and Solbiati, L. (2015). Real-time US-CT/MRI image fusion for guidance of thermal ablation of liver tumors undetectable with US: results in 295 cases. Cardiovascular and Interventional Radiology, 38(1), pp. 143-151.

Mulier, S., Ni, Y., Jamart, J., Ruers, T., Marchal, G., and Michel, L. (2005). Local recurrence after hepatic radiofrequency coagulation: multivariate meta-analysis and review of contributing factors. Annals of Surgery, 242(2), pp. 158-171.

Napoli, A., Anzidei, M., Ciolina, F., Marotta, E., Cavallo Marincola, B., Brachetti, G., Mare, L. D., Cartocci, G., Boni, F., Noce, V. Bertaccini, L., and Cataloano, C.(2013). MR-guided high-intensity focused ultrasound: Current status of an emerging technology. Cardiovascular and Interventional Radiology, 36(5), pp. 1190-1203.

Natale, A., Pisano, E., Shewchik, J., Bash, D., Fanelli, R., Potenza, D., Santarelli, P., Schweikert, R., White, R., Saliba, W., Kanagaratnam, L., Tchou, P., and Lesh, M. (2000). First human experience with pulmonary vein isolation using a through-the-balloon circumferential ultrasound ablation system for recurrent atrial fibrillation. Circulation, 102(16), pp. 1879-1882.

Nishikawa, H., Kimura, T., Kita, R., and Osaki, Y. (2013). Radiofrequency ablation for hepatocellular carcinoma. International Journal of Hyperthermia, 29(6), pp. 558-568.

O'Connor, C. M., Adams, J. U., and Fairman, J. (2010). Essentials of Cell Biology. NPG Education, Cambridge.

O'Reilly, M. A., and Hynynen, K. (2015). Emerging non-cancer applications of therapeutic ultrasound. International Journal of Hyperthermia, 31(3), pp. 310-318.

Ozisik, M. N. (1993). Heat Conduction. John Wiley and Sons, Chap. 6, pp. 222-223.

Pereira, P. L., Truubenbach, J., Schenk, M., Subke, J., Kroeber, S., Schaefer, I., Remy, C. T., Schmidt, D., Brieger, J., and Claussen, C. D. (2004). Radiofrequency ablation: in vivo comparison of four commercially available devices in pig livers 1. Radiology, 232(2), pp. 482-490.

Petrowsky, H., and Busuttil, R. W. (2008). Resection or ablation of small hepatocellular carcinoma: What is the better treatment? Journal of Hepatology, 49(4), pp. 502-504.

Salgaonkar, V. A., and Diederich, C. J. (2015). Catheter-based ultrasound technology for image-guided thermal therapy: Current technology and applications. International Journal of Hyperthermia, 31(2), pp. 203-215.

Sapareto, S. A., and Dewey, W. C. (1984). Thermal dose determination in cancer therapy. International Journal of Radiation Oncology Biology Physics, 10(6), pp. 787-800.

Scheffer, H. J., Nielsen, K., van Tilborg, A. A. J. M., Vieveen, J. M., Bouwman, R. A., Kazemier, G., Niessen H. W. M., Meijer, S., van Kuijk, C., van den Tol, M. P., Meijernik, M. R., and Meijerink, M. R. (2014). Ablation of colorectal liver metastases by irreversible electroporation: results of the COLDFIRE-I ablate-and-resect study. European Radiology, 24(10), pp. 2467-2475.

Schmidt, B., Antz, M., Ernst, S., Ouyang, F., Falk, P., Chun, J. K., and Kuck, K. H. (2007). Pulmonary vein isolation by high-intensity focused ultrasound: first-in-man study with a steerable balloon catheter. Heart Rhythm, 4(5), pp. 575-584.

Schmidt-Neilsen, K. (1946). Melting points of human fats as related to their location in the body. Acta Physiologica Scandinavica, 12(2-3), pp. 123-129.

Shetty, S. V., and Chopra, S. (2015). Therapeutic Intra Vascular Ultrasound (TIVUS). In Renal Denervation (pp. 91-96). Springer London.

Siegel, R. L., Miller, K. D., and Jemal, A. (2015). Cancer statistics, 2015. CA: A Cancer Journal for Clinicians, 65(1), pp. 5-29.

Simon, C. J., Dupuy, D. E., and Mayo-Smith, W. W. (2005). Microwave ablation: principles and applications 1. Radiographics, 25, pp. S69-S83.

Subramanian, S., Rudich, S. M., Alqadah, A., Karunakaran, C. P., Rao, M. B., and Mast, T. D. (2014). In vivo thermal ablation monitoring using ultrasound echo decorrelation imaging. Ultrasound in Medicine and Biology, 40(1), pp. 102-114.

Szabo, T. L. (2004). Diagnostic Ultrasound Imaging: Inside Out. Academic Press.

ter Haar, G. (2007). Therapeutic applications of ultrasound. Progress in Biophysics and Molecular Biology, 93(1), pp. 111-129.

Timberlake, K. C. (2014). Chemistry: An Introduction to General, Organic, and Biological Chemistry (Ch. 15). Pearson Higher Ed.

Wu, H., Exner, A. A., Shi, H., Bear, J., and Haaga, J. R. (2009). Dynamic evolutionary changes in blood flow measured by MDCT in a hepatic VX2 tumor implant over an extended 28-day growth period: time-density curve analysis. Academic Radiology, 16(12), pp. 1483-1492.

Zervas, N. T. and Kuwayama, A. (1972). Pathological characteristics of experimental thermal lesions: comparison of induction heating and radiofrequency electrocoagulation. Journal of Neurosurgery, 37(4), pp. 418-422.

Zhang, S., Wan, M., Zhong, H., Xu, C., Liao, Z., Liu, H., and Wang S. (2009). Dynamic changes of integrated backscatter, attenuation coefficient and bubble activities during high-intensity focused ultrasound (HIFU) treatment. Ultrasound in Medicine and Biology, 35(11), pp. 1828-1844.